# Experimental System for Validating GPS/INS Integration Algorithms

NIKLAS HJORTSMARKER


FOI-R--1875--SE Scientific report
ISSN-1650-1942 December 2005

**Systems Technology**

FOI is an assignment-based authority under the Ministry of Defence. The core activities are research, method and technology development, as well as studies for the use of defence and security. The organization employs around 1350 people of whom around 950 are researchers. This makes FOI the largest research institute in Sweden. FOI provides its customers with leading expertise in a large number of fields such as security-policy studies and analyses in defence and security, assessment of different types of threats, systems for control and management of crises, protection against and management of hazardous substances, IT-security an the potential of new sensors.

FOI
Swedish Defence Research Agency
SE-164 90 STOCKHOLM

Tel: +46 8 5550 3000
Fax: +46 8 5550 3100

www.foi.se

Niklas Hjortsmarker

# Experimental System for Validating GPS/INS Integration Algorithms

FOI-R--1875--SE Scientific report **Systems Technology**
ISSN-1650-1942 December 2005

| | | |
|---|---|---|
| **Issuing organisation**<br>FOI – Swedish Defence Research Agency<br>Systems Technology<br>SE-164 90 STOCKHOLM | **Report number, ISRN**<br>FOI-R--1875--SE | **Report type**<br>Scientific report |
| | **Research area code**<br>Strike and Protection | |
| | **Month year**<br>December 2005 | **Project no.**<br>E6060 |
| | **Sub area code**<br>Weapons and Protection | |
| | **Sub area code 2** | |
| **Author/s (editor/s)**<br>Niklas Hjortsmarker | **Project manager**<br>Bengt Boberg | |
| | **Approved by**<br>Monica Dahlén | |
| | **Sponsoring agency**<br>FM | |
| | **Scientifically and technically responsible**<br>Fredrik Berefelt | |


**Report title**
Experimental System for Validating GPS/INS Integration Algorithms


**Abstract**
The work in this master thesis mainly consists of the design and implementation of an experimental platform for logging navigation data. Data from a Micro Electro Mechanical System (MEMS) Inertial Mmeasurement Unit (IMU) of the type MICRO ISU BP3010 and a Superstar II GPS receiver are used for validation and evaluation of robust navigation algorithms.
The report first briefly describes the theory of integration of GPS and INS. Then the implemented test equipment and the used navigation sensors are presented. Experiments were conducted in both high- and low-dynamic environments, using a roller coaster and a car respectively. Two different integration algorithms, tight and loose integration, are validated with data from the low dynamic car case.
Laboratory tests have been performed for the MEMS IMU to determine its deterministic and stochastic errors. The tests consisted of drift test, gyro-turn-table tests and up-down tests. Both spectral analysis and Allan variance analysis has been used and compared while determining the stochastic errors.
Results from car-tests shows that the tightly coupled navigation algorithm works better than the loosely coupled and in particular when less than 4 satellites.



**Keywords**
Sensor Integration, Navigation, GPS, Inertial Navigation, MEMS, Experiment, Calibration, Allan Variance, Spektral Analysis

| | |
|---|---|
| **Further bibliographic information** | **Language** English |
| **ISSN** ISSN-1650-1942 | **Pages** 78 p. |
| | **Price acc. to pricelist** |

| | | |
|---|---|---|
| **Utgivare**<br>FOI – Totalförsvarets forskningsinstitut<br>Systemteknik<br>164 90 STOCKHOLM | **Rapportnummer, ISRN**<br>FOI-R--1875--SE | **Klassificering**<br>Vetenskaplig rapport |
| | **Forskningsområde**<br>Bekämpning och skydd | |
| | **Månad år**<br>December 2005 | **Projektnummer**<br>E6060 |
| | **Delområde**<br>VVS med styrda vapen | |
| | **Delområde 2** | |
| **Författare/redaktör**<br>Niklas Hjortsmarker | **Projektledare**<br>Bengt Boberg | |
| | **Godkänd av**<br>Monica Dahlén | |
| | **Uppdragsgivare/kundbeteckning**<br>FM | |
| | **Tekniskt och/eller vetenskapligt ansvarig**<br>Fredrik Berefelt | |
| **Rapportens titel**<br>Experimentellt system för validering av GPS/INS integrerings algoritmer | | |



**Sammanfattning**

Examensarbetet innefattar huvudsakligen design och implementation av en experimentell plattform för loggning av navigeringsdata. Data från en MEMS IMU (eng. Micro Electro Mechanical System, Inertial Measurement Unit) av typen MICRO ISU BP3010 och en Superstar II GPS mottagare har använts för att validera och evaluera robusta navigeringsalgoritmer.

Rapporten beskriver övergripande teorin bakom integration av GPS och ett tröghetsnavigeringssystem (TNS). Sedan presenteras de sensorer som används. Experiment utfördes både i hög och lågdynamiska miljöer. Det högdynamiska experimentet utfördes i en berg-och-dalbana och det lågdynamiska utfördes med en personbil. Två integrations algoritmer, tät och lös integration, validerades med hjälp av datat från det lågdynamiska experimentet med bil.

Tester av MEMS sensorerna utfördes i laboratoriemiljö då deterministiska och stokastiska fel bestämmdes. Spektral analys och Allan varians analys har använts och jämförts vid bestämning av de stokastiska felen.

Resultaten från bil-försöken visar att den tätt kopplade navigerings algoritmen fungerar bättre än den löst kopplade och speciellt då det finns färre än fyra satelliter tillgängliga.



**Nyckelord**

Sensor Integration, Navigering, GPS, Tröghetsnavigering, MEMS, Experiment, Kalibrering, Allan Varians, Spektral Analys

| | |
|---|---|
| **Övriga bibliografiska uppgifter** | **Språk** Engelska |
| **ISSN** ISSN-1650-1942 | **Antal sidor:** 78 s. |
| **Distribution enligt missiv** | **Pris: Enligt prislista** |

# Contents

# Contents

# 1 Introduction

## 1.1 Background

Many civil and military systems require robust and exact position and time and therefore based on Global Navigation Satellite System (GNSS). Today GPS is the most commonly used GNSS but 2008-2010 Galileo, a European equivalent system, will be in operation. An unsupported GPS-based navigation systems is very sensitive because of the weak satellite signals. Inertial Navigation Systems (INS) on the other hand is self contained. The position of the vehicle is calculated using measurements of accelerations and angular velocities in three dimensions. INS is therefore a robust and jamming resistant navigation sensor. However the position error of an INS increases without bounds due to the integration of measurement errors in the accelerometers and gyros. The GPS delivers positions at a slower rate, typically a few times per second, and the position error is bounded. These complementary properties make it suitable to integrate INS and GPS to get accurate and reliable positions. Why use a jamming sensitive GPS at all? Why not use a high class INS?

By integration of INS and GPS one can achieve better performance for less money. The performance of a low cost stand alone MEMS IMU, does not currently fit into tactical grade requirements. But being aided by GPS, tactical grade navigation performance can be achieved. A Cheap and small navigation system like a MEMS INS/GPS integration makes it possible for military troops and smaller units to get access to good positioning and navigation functions.

The drawback of traditional advanced high performing and robust military navigation systems is that they are expensive, bulky and power consuming. By integrating a GPS receiver and a MEMS (Micro Electro Mechanical System) based IMU (Inertial Measurement Unit) one can achieve a navigation system of small size and weight, with modest power consumption and cost.

However, the error characteristic of the MEMS sensors is often highly nonlinear and temperature dependent. To achieve the desired accuracy it is therefore crucial to determine and model the dominating errors and analyzing their effects in navigation applications.

## 1.2 Aim Of Work

The department of Autonomous Systems at the Swedish Defence Research Agency (FOI) conduct research on robust navigation. This include areas such as integrated navigation systems and collaborative navigation [14][17]. Often experimental systems are desired to validate navigation algorithms through experiments. In this assignment the design of an experimental integrated navigation system is proposed. Such a system could also be used as a reference system when using less accurate sensors to evaluate new navigation algorithms. The objective of this master thesis should be to create an integrated navigation platform based on an IMU (Inertial Measurement Unit, three accelerometers and three gyros) and a GPS-receiver. Experiments should be performed to

evaluate and validate the navigation system as well as existing navigation algorithms. The data collected during experiments should be used in Matlab to integrate the IMU-signals by using the navigation equations to obtain position, velocity and orientation of the navigation platform. The result should then be compared with a GPS position solution. Next step is then to implement both a loosely-coupled and a tightly coupled Kalman filter based on the GPS and IMU signals. The work consist of:

- Mounting and installing the experimental equipment: IMU, GPS, computers, power supply, data logger.
- Programming data logging software to store and time stamp the IMU and GPS-data.
- Performing functionality tests of the separate sensor systems and the total system.
- Testing IMU in laboratory environment by using the FOI rate table and performing up-down test on the accelerometers.
- Determining dominating IMU-errors by using and comparing both power spectral density analysis and Allan variance analysis.
- Planning and performing of experiments both in a high (roller coaster) and low (car) dynamics environment.
- Validation and comparison of two navigation algorithms, the loosely and tightly coupled Kalman filter at a $1Hz$ measurement update rate.

A part of the assignment has also been to document the software and the hardware of the navigation system, the experimental results and the models. The IMU used in the experiment was a MICRO-ISU BP3010, which is a Micro Electro Mechanical Sensor (MEMS) based on MEMS accelerometers and gyros from Analog Devices. It is a small light weighted and relatively cheap IMU-sensor unit. The GPS-receiver was a Superstar II from Novatel with 10Hz update rate.

# 2 Inertial Navigation

## 2.1 Introduction

Inertial navigation is based on calculating position, velocity and orientation of a moving vehicle by using measurements from inertial sensors, such as accelerometers and gyros. Inertial sensors detect and measure motion based on the law's of nature and do not rely on external signals, this makes inertial navigation robust and difficult to jam.

Inertial navigation is based on Newton's laws of motion.

$$\mathbf{F} = \frac{d}{dt}\left(m\dot{\mathbf{x}}\right) \tag{2.1}$$

where $\mathbf{F}$ is the sum of applied forces, gravity excluded, on a body with constant mass $m$ and position $\mathbf{x}$. Equation 2.1 needs to be modified to account for the earth's gravitational field where $\mathbf{g}$ is the gravitational acceleration vector.

$$m\ddot{\mathbf{x}} = \mathbf{F} + m\mathbf{g} \tag{2.2}$$

The acceleration due to an applied force is $\mathbf{a} = \frac{\mathbf{F}}{m}$, substituting that in equation 2.2 becomes

$$\ddot{\mathbf{x}} = \mathbf{a} + \mathbf{g} \tag{2.3}$$

These equations only hold for the Newtonian inertial frame. If we now look at the equation in the $i$-frame, 2.3 becomes

$$\ddot{\mathbf{x}}^{\mathbf{i}} = \mathbf{g}^{\mathbf{i}}\left(\mathbf{x}^{i}\right) + \mathbf{a}^{i} \tag{2.4}$$

where $\mathbf{x}^i$ is the position in the $i$-frame, $\mathbf{g}^i$ is the acceleration due to the gravitational field in the $i$-frame and depends on the position. $\mathbf{a}^i$ is the specific force sensed by the accelerometers. These equations is solved for the position $\mathbf{x}^i$ and velocity.

## 2.2 Coordinate Frames

### 2.2.1 Inertial Frame

An inertial frame is a reference frame in which Newton's laws of motion holds. The origin of the inertial frame and the orientation of the inertial coordinate axes are arbitrary. For convenience, the Inertial frame is often defined so that it coincides with the earth's centre of mass. This frame will be called the i-frame and should not be confused with the ideal inertial frame. All inertial measurements is relative to this frame. Coordinates in this frame will be denoted with superscript $i$ as $x^i$.

### 2.2.2 Earth Centred Earth Fixed Frame

The Earth Centred Earth Fixed (ECEF) frame has its origin in the earth's centre of mass. It is defined with the x-axis pointing towards the intersection

of the Greenwich meridian and the equator. The z-axis along the earth's rotation axis and the y-axis in the direction that forms a right handed orthogonal coordinate system. Coordinates in this frame will be denoted with superscript $e$ as $x^e$.

### 2.2.3 Navigation Frame

The navigation frame is commonly used to describe the navigation of a vehicle in a local coordinate frame, to provide local directions north, east and down. Therefor the axes of the frame is defined in these directions (NED), another definition of the navigation frame is ENU. The down direction is defined from the down direction of a local tangent plane and therefor it does not always coincide with the direction of earth's centre. Coordinates in this frame will be denoted with superscript $n$ as $x^n$.

### 2.2.4 Body Frame

The body frame is rigidly attached to the navigating vehicle, and it is moving and rotating with the vehicle. The axes are defined as forward, right and down. The objective of navigation is to determine the position and attitude of a vehicle based on measurements from sensors attached to the vehicle. This motivates the use of body frame. Coordinates in this frame will be denoted with superscript $b$ as $x^b$.

## 2.3 Navigation Equations

Let the $a$-frame be an arbitrary frame that rotates with respect to the $i$-frame with angular rate $\omega_{ia}^a$. A vector in the $a$-frame can be expressed in coordinates of the $i$-frame, by

$$\mathbf{x}^i = C_a^i \mathbf{x}^a \tag{2.5}$$

Where $C_a^i$ is the transformation matrix from the $a$-frame to the $i$-frame. The time derivative of this matrix is given by (see [13])

$$\dot{C}_a^i = C_a^i \Omega_{ia}^a \tag{2.6}$$

Where $\Omega_{ia}^a$ denotes a skew-symmetric matrix with elements from $\omega_{ia}^a = (\omega_1, \omega_2, \omega_3)$ according to

$$\Omega_{ia}^a = \begin{pmatrix} 0 & -\omega_3 & \omega_2 \\ \omega_3 & 0 & -\omega_1 \\ -\omega_2 & \omega_1 & 0 \end{pmatrix} \tag{2.7}$$

To obtain the second time derivative, we use the chain rule. the second time derivative then becomes

$$\ddot{C}_a^i = C_a^i \dot{\Omega}_{ia}^a + C_a^i \Omega_{ia}^a \Omega_{ia}^a \tag{2.8}$$

Differentiating 2.5 twice with respect to time using 2.6 and 2.8 yields

$$\begin{aligned} \ddot{\mathbf{x}}^i &= \ddot{C}_a^i \mathbf{x}^a + 2\dot{C}_a^i \dot{\mathbf{x}}^a + C_a^i \ddot{\mathbf{x}}^a \\ &= C_a^i \ddot{\mathbf{x}}^a + 2C_a^i \Omega_{ia}^a \dot{\mathbf{x}}^a + C_a^i \left( \dot{\Omega}_{ia}^a + \Omega_{ia}^a \Omega_{ia}^a \right) \mathbf{x}^a \end{aligned} \tag{2.9}$$

Solving for $\ddot{\mathbf{x}}^a$ and combining with 2.4 and using the orthogonality of $C_a^i$ gives the system dynamics for the position in the $a$-frame

$$\ddot{\mathbf{x}}^a = -2\Omega_{ia}^a \dot{\mathbf{x}}^a - \left( \dot{\Omega}_{ia}^a + \Omega_{ia}^a \Omega_{ia}^a \right) \mathbf{x}^a + \mathbf{a}^a + \mathbf{g}^a \tag{2.10}$$

Where $\mathbf{a}^a = C_i^a \mathbf{a}^i$ and $\mathbf{g}^a = C_i^a \mathbf{g}^i(\mathbf{x}^i)$. The system (2.10) of three second order differential equations can be transformed into a system of six first order differential equations, this gives the navigation equations in an arbitrary frame ($a$-frame).

$$\begin{array}{l} \frac{d}{dt}\dot{\mathbf{x}}^a = -2\Omega_{ia}^a \dot{\mathbf{x}}^a - \left(\dot{\Omega_{ia}^a} + \Omega_{ia}^a \Omega_{ia}^a\right)\mathbf{x}^a + \mathbf{a}^a + \mathbf{g}^a \\ \frac{d}{dt}\mathbf{x}^a = \dot{\mathbf{x}}^a \end{array} \tag{2.11}$$

## 2.4 Navigation Equations in $e$-frame

To obtain the navigation equations in the $e$-frame, one can draw knowledge from the fact that difference between the $i$-frame and the $e$-frame is only rotation around the third axis in the $e$-frame. The rotation around the third axis is the earth rotation rate. Since the earth rotation rate is constant, $\dot{\Omega}_{ie}^e = 0$, we obtain from (2.11) the navigation equations in the $e$-frame.

$$\begin{array}{l} \frac{d}{dt}\dot{\mathbf{x}}^e = -2\Omega_{ie}^e \dot{\mathbf{x}}^e - \Omega_{ie}^e \Omega_{ie}^e \mathbf{x}^e + \mathbf{a}^e + \mathbf{g}^e \\ \frac{d}{dt}\mathbf{x}^e = \dot{\mathbf{x}}^e \end{array} \tag{2.12}$$

where

$$\Omega_{ie}^e = \begin{pmatrix} 0 & -\omega_e & 0 \\ \omega_e & 0 & 0 \\ 0 & 0 & 0 \end{pmatrix} \tag{2.13}$$

and $\omega_e$ is the earth rotation rate.
$\mathbf{a}^e$ is computed from sensed accelerometer data in the body frame

$$\mathbf{a}^e = C_b^e \mathbf{a}^b \tag{2.14}$$

where the transformation, $C_b^e$, is determined by integrating the angular rates obtained from the gyro data.

$$\dot{C}_b^e = C_b^e \Omega_{eb}^b \tag{2.15}$$

Where the components of $\Omega_{eb}^b$ can be expressed in terms of sensed angular rates, $\omega_{ib}^b$, from the gyros as

$$\omega_{eb}^b = \omega_{ib}^b - C_e^b \omega_{ie}^e \tag{2.16}$$

The equations (2.12)-(2.16) define first order differential equations for the navigation states consisting of position, velocity and attitude driven by the IMU-signals $\mathbf{a}^b$ and $\omega_{ib}^b$. If $\mathbf{x}$ denotes the total navigation state and $\mathbf{a}$ denotes the IMU-signals (both $\mathbf{a}^b$ and $\omega_{ib}^b$) these differential equations may be written s

$$\dot{\mathbf{x}}(t) = f(\mathbf{x}(t), \mathbf{a}(t)) \tag{2.17}$$

This equation will be referred to as the *navigation equations.*

# 3 INS and GPS Integration

The main idea of integrated navigation systems is to take advantage of the complementary attributes of two or more navigation systems to get a system that provides greater precision than either of the system components operating stand alone. INS and GPS really complement each other, both have large advantages as well as disadvantages. An INS exhibits relatively low noise, but drifts over time. This is because the position solution is based on the integration of accelerometer and gyro sensor measurements. Errors introduced in the measurements, such as biases and noisy sensor data, will accumulate and result in an unbounded position error. The GPS on the other hand produce position with a bounded error, which depends on the quality of the GPS receiver. The drawback of GPS is that it relies on weak satellite signals, causing poor GPS-performance or total GPS-outage in urban environments, in tunnels, under water and in forests with heavy foliage. Moreover, there is a great risk of jamming the GPS receiver. More about navigation warfare, see [14].Table 3.1 shows the main features of inertial and satellite navigation systems. Due to the complementary features, GPS and INS are ideal to integrate. A number of different integration architectures have been developed to allow GPS and INS to be combined. There are four main classes of integration architecture

- Uncoupled systems
- Loosely coupled systems
- Tightly coupled systems
- Deep/Ultra-tightly coupled systems

Figure 3.1 illustrates the advantage of integrating GPS and INS.

## 3.1 System Architectures

### 3.1.1 Uncoupled Systems

This is the simplest method of integrating GPS and INS. The two systems operate independently, when a GPS position and/or velocity measurement is available the INS is reset. This bounds the error growth of the position and velocity estimates in the INS. This method does not provide performance enhancement and jamming avoidance like the coupled architectures.

### 3.1.2 Loosely Coupled Integration

Loosely coupled systems or decentralised systems are simple and an effective way of integrating GPS and INS. The GPS operates autonomously ,whilst providing measurement updates to the inertial system. Figure 3.2 shows a simplified representation of a loosely coupled system integration architecture.

The main advantages of loosely coupled integration is the simplicity and redundancy. The main problem with loosely coupled integration is the cascade-coupled Kalman filters, where the position noise from the GPS receiver can be coloured.This may create problems depending on for example update rates.

### 3.1.3 Tightly Coupled Integration

Tightly coupled or centralised integration uses the pseudoranges (and possibly the phase of the carrier frequency) from the GPS receiver. The main advantages of the tightly coupled integration is that only one Kalman filter is used so the problem with coloured noise does not arise. The system does not require a full GPS solution (tracking of four satellites) to aid the INS. Even GPS data from only one or a few satellites will now contribute enough information to the navigation filter to estimate the IMU-errors and thereby bounding the navigation errors. The accuracy of course improve with the number of visible satellites. Figure 3.3 shows a simplified representation of a tightly coupled integration architecture.

## 3.2 Integrating GPS and MEMS-IMU

According to [18] there are four grades of IMU:s,Strategic, Navigation, Tactical and Consumer grade, see Table 3.2. Accurate IMU:s are expensive and bulky. However the performance of a low cost stand alone MEMS IMU does not fit into Tactical grade requirements. But being aided by GPS, Tactical grade navigation grade performance of MEMS INS/GPS integration can be achieved [10]. Figure 3.4 shows an example of a aircraft travelling in an ideal horizontal flight from point $A$ to point $B$ using a Tactical Grade Inertial System, with gyro drifts of $10^\circ/h$ . After 1 hour flight, arriving at point $B$, the Position Error (PE) should be 40 $km$ at most. Figure 3.5 shows a possible flight navigation profile for an aircraft equipped whit a MEMS INS/GPS Navigation system. To maintain a Tactical Grade performance using a Consumer Grade gyro, GPS corrections needs to be applied during the flight. In this example the INS needs at least 10 GPS corrections to maintain a Tactical Grade performance. The example is taken from [10]. This example shows that, even though using a cheap Consumer grade MEMS gyro, one can achieve better performance by GPS/INS integration. Thus a low cost navigation system can be built with sufficient accuracy.

Table 3.1: Comparison of features of inertial and satellite navigation systems.

| | Advantages | Disadvantages |
|---|---|---|
| Inertial navigation Systems (INS) | High data rate.<br>Provides both translational and rotational data.<br>Autonomous-Jamming insensitive. | Unbounded errors.<br>Knowledge of gravity required. |
| Global Navigation Satellite System (GNSS) | Errors are bounded. | Low data rate.<br>No attitude information.<br>Sensitive to jamming- intentional and unintentional. |

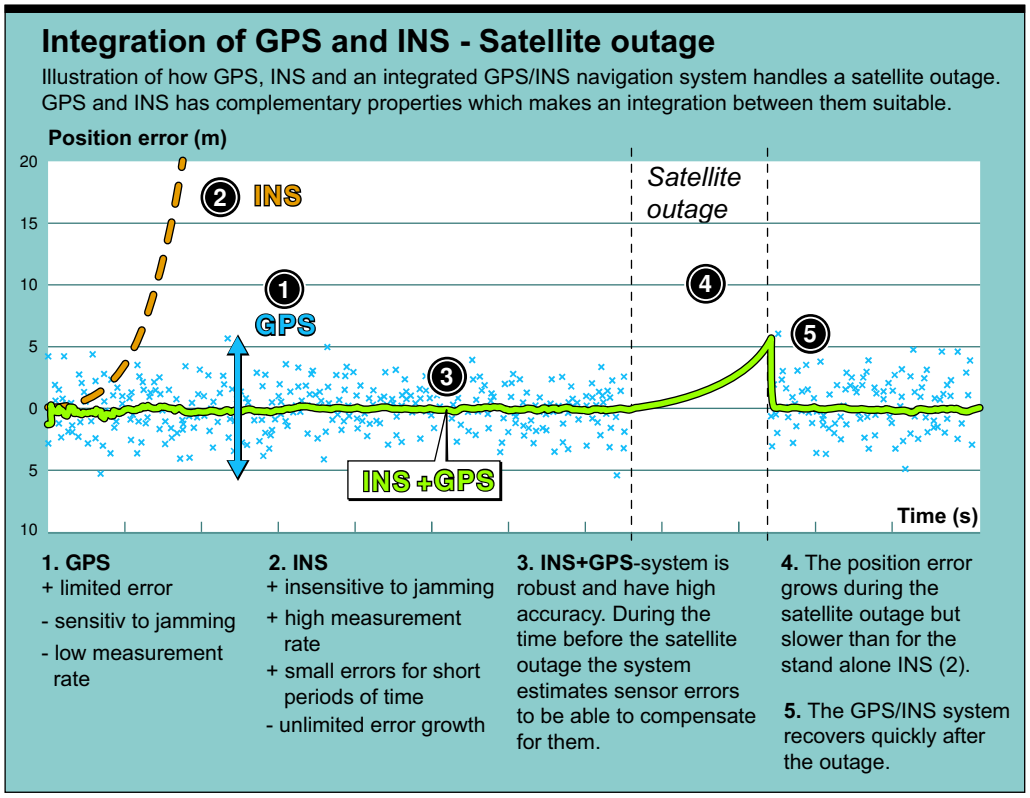


Figure 3.1: Integration of GPS and INS overview

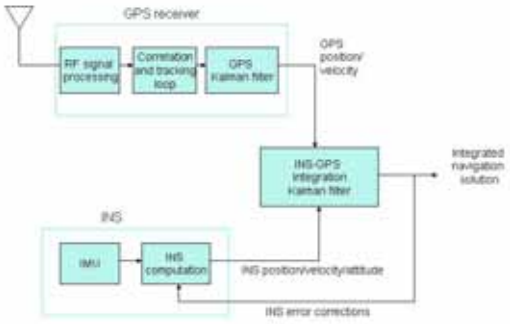


Figure 3.2: Loosely coupled INS-GPS integration architecture

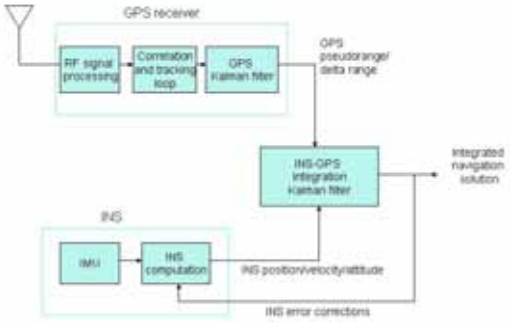


Figure 3.3: Tightly coupled INS-GPS integration architecture

Table 3.2: The table describes Position, Gyro and Accelerometer errors for different grades of INS.

| Inertial System Grade | Position Error $[km/h]$ | Gyro Error $[^\circ/h]$ | Accelerometer Error $[mg]$ |
|---|---|---|---|
| Strategic | <0.03 | 0.0001 | 0.001 |
| Navigation | <4 | 0.015 | 0.1 |
| Tactical | 18.5 *to* 40 | 1 *to* 10 | 1.0 |
| Consumer | >40 | 1000 | 20 |

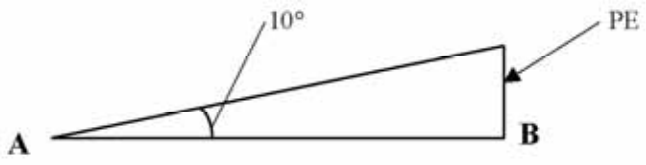


Figure 3.4: Growth of the performance error of a Tactical Grade INS, for a one hour flight.

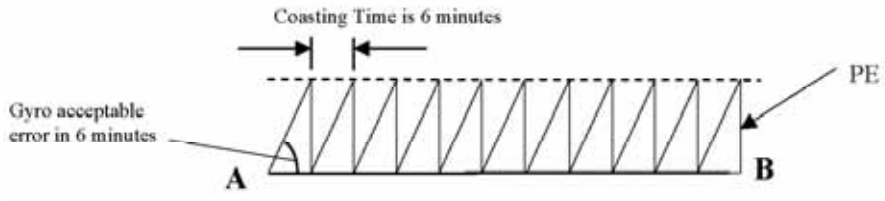


Figure 3.5: MEMS INS/GPS Tactical Grade Performance

# 4 Equipment

The experiment equipment consists of navigation sensors, reference system and a data logger.

## 4.1 Navigation Sensors

The navigation sensors are small and cheap. The first is a Micro Electronic-Mechanical System (MEMS) IMU and the second a GPS receiver.

### 4.1.1 MEMS IMU

The MEMS IMU used is a MICRO-ISU BP3010 from BEC Navigation System and costs about 1600 euro. The size of the sensor can be compared to one-euro coin see Figure 4.1 and Table 4.1 shows the technical specifications given from the manufacturer. The IMU are here strapped down to the navigating vehicle and the measurements consists of angular increments and velocity increments from the three gyros and three accelerometers respectively. The measurements are transmitted via RS232 and in addition the IMU produces a check flag that signals if the measurements are valid. The MICRO-ISU BP3010 consists of


Figure 4.1: The MICRO-ISU BP3010 with socket for RS232 communication interface. The size can be compared with the 1 euro coin.

three ADXRS 300 gyros from Analog Devices with a range of $\pm 300°/s$, the internal sampling rate is $40\,Hz$ and the manufacturer given noise performance is $0.1 deg/s/\sqrt{Hz}$. The Accelerometers are two ADXC 210E from Analog Devices which are a dual accelerometer with a range of $\pm 10g$ with an internal sampling rate of $6kHz$ with a given noise performance of maximum $1000\mu g/s/\sqrt{Hz}$. The accelerometers and gyros are controlled by 3 micro- controllers. The MICRO-ISU BP3010 is precompensated for gyro and accelerometer scale factor errors, bias errors and misalignment errors. In addition to the precompensated cali-

Table 4.1: Technical specifications for MICRO-ISU BP3010

| | |
|---|---|
| Physical dimensions | 35 mm x 22 mm x 12 mm |
| Weight | 30 g approximately |
| Power consumption | 0.5 Watt |
| Scale factor accuracy | 0.2 % |
| Residual bias errors | $0.5°/s$ (gyro), 5 mg (accel) |
| Misalignment error | $<0.1°$ |
| Output noise (rms) | 0.03°, 0.005 m/s |
| Bandwidth | $\geq 32Hz$ |
| Shock | 1000 g, 10 ms half-sine |

brated values the MICRO-ISU BP3010 compensate for temperature dependent scale factors and biases as well as coning and sculling effects [18].

The MICRO-ISU BP3010 used in the this navigation system is one of the first produced units from BEC Navigation Systems that has been borrowed from SAAB Bofors Dynamics AB. Since the unit is one of the first produced, BEC Navigation Systems can not assure that the given specifications are valid. The calibration and compensation procedure has been improved since the first units. For more information about the MICRO-ISU BP3010 see [8].

### 4.1.2 GPS Receiver

The other navigation sensor is a Novatel Superstar II GPS receiver, Figure 4.2, which is capable of delivering raw measurements (carrier phase and code phase) with 10 Hz, a position estimate with 1 Hz and satellite ephemeris data. Other messages can also be received see [2]. Table 4.2 shows the technical specifications. The measurements are transmitted via RS232. For further

Figure 4.2: Novatel Superstar II receiver card

information about the receiver and the different messages see [2].

## 4.2 GPS Reference System

To be able to validate the performance of the navigation filters it is crucial to have some kind of reference system. Whether it is a carrier phase based GPS, a very accurate predefined testing track or a high class IMU.

| Position accuracy | |
|---|---|
| Single point L1 | $< 5$ m CEP |
| WAAS L1 | $<1.5$ m CEP |
| DGPS (L1 C/A) | $<1$ m CEP |
| Measurement Precision | |
| L1 C/A code | 75 cm rms |
| L1 carrier phase | 1 cm rms |

Table 4.2: Technical specifications for Novatel Superstar II receiver

### 4.2.1 Multi Antenna GPS Attitude System

The reference system used is a Javad HD2 GPS receiver, Fig 4.3, used together with a Trimble 3400 base station. The Javad HD2 GPS receiver is an attitude


Figure 4.3: Javad HD2 GPS receiver

measuring GPS. The unit consists of two receiver cards and two antennas, enabling two angles to be measured, the attitude is calculated using the carrier phase of the GPS signal. The two Javad antennas were mounted on the aluminium pole with 1.5 m separation, see Fig 4.4. The pole is then strapped

Figure 4.4: Javad antenna mounting

down to the car allowing the pitch and heading of the car to be estimated. In table 4.3 and 4.4 the technical specifications of the reference system can be seen. Mounting the antennas with a 1.5 m separation will result in 0.15°

Table 4.3: Real time position accuracy for Javad HD2

| Autonomous | Carrier phase differential |
|---|---|
| $\sim 3.0$ m 3D RMS | $\sim 0.01$ m 3D RMS |

heading accuracy and 0.31° pitch accuracy. The attitude has been used mainly

Table 4.4: Real time attitude accuracy for Javad HD2. Where L is the separation between the antennas in meters.

| Heading | Roll/Pitch |
|---|---|
| $\sim 0.004/L$ rad RMS | $\sim 0.008/L$ rad RMS |

at the initialization of the system. Generally it is always good to be able to validate the navigation filter with as good reference measurements as possible and in particular using the attitude. The Javad HD2 receiver system was very sensitive to vibrations and accelerations resulting in severe measurement outages. The manufacturer reluctantly informs that the oscillator mounting will be improved in later models. The downside of using a GPS based reference system is that the reference system relies on the same satellite measurements as in the filter. If the satellites has a bad geometrical constellation, the DOP (Dilution of Precision) is high, this will effect both the filter accuracy as well as the reference accuracy.

## 4.3 Data Logger

The data logger consists of PC104 running Debian Linux and an interrupt driven software. It is used to time stamp and store the data from the navigation sensors.

### 4.3.1 Software

The data logger software is an interrupt driven threaded C++ implementation, which creates a thread for each attached sensor, here the Superstar II GPS receiver and the MICRO-ISU BP3010. The thread associated with the Superstar II GPS runs a function called *gpslogger* that first opens a file where all the GPS data will be stored. The *gpslogger* function then creates a GPS-logger object which opens a serial port on the PC104 and initiate the GPS receiver. The GPS-logger object then initialises the receiver by setting the desired messages to be received. When the GPS-logger object is created the function sets serial port filedescriptor (FD) to interrupts, when a interrupt comes the serial port data is read. When the serial port is read a header in the serial port data is searched for. When a valid header is found the message is time stamped by the system time and stored binary in the associated file. Figure 4.5 shows a flow diagram of the GPS-logger thread.

The IMU-logger thread works in a similar way as the GPS-logger. They differ in the initialisation where the IMU-logger thread do not require initialisation of witch messages that should be received. The data logger is terminated by pressing Ctrl-Z. The interrupt handler then closes the binary files, serial ports and terminates the logger threads.

The message format of the binary files are as the original messages with the difference that the message is time stamped by a 8 byte float. The binary message consists of, in order: the header, the time stamp and finally the message. For further information about message and header information for the Superstar II GPS receiver see [2].

### 4.3.2 Sensor Synchronisation and Timing Aspects

The data from the two sensors is time stamped according to 4.3.1. That means that every sensor sample has a time stamp with system time. In addition to the system time all GPS samples has a GPS-time stamp. It is assumed that the

internal sampling of the IMU of 64 $Hz$ is stable. The sensors is then synchronised by taking the difference in system time of the first samples from the two sensors. The difference is then subtracted from the GPS-time of the first GPS sample, leading to the IMU start time. Knowing that the internal sample rate of the IMU is 64 $Hz$, the next IMU sample has the GPS-time: $start\,time + \frac{1}{64}$. The filters use the GPS-time stamp to synchronise the measurements.
Since the measurements is not sampled at exactly the same time the measurement update (observation) in the filter will not be at the same time as the time update (prediction). This problem can be solved in several ways, one solution is to interpolate the IMU measurements so an estimate of the IMU measurements is available at exactly the same time as the observation. The implemented solution is to disregard this problem and associate the observation with the prediction closest in time. This solution will introduce errors and the error will be velocity dependent. In the case of an IMU with sampling time of 64 $Hz$ the largest time difference between a prediction and an observation is $1/64\,s$. This means that the vehicles position can be off with $\frac{1}{64} \cdot v$ between successive samples due to problem with time synchronization, where $v$ is the velocity of the vehicle. But even if the vehicle should reach a speed of $100\,m/s$ the position error should only be <1.6 $[m]$, which is included in the covariance matrix of the observation.

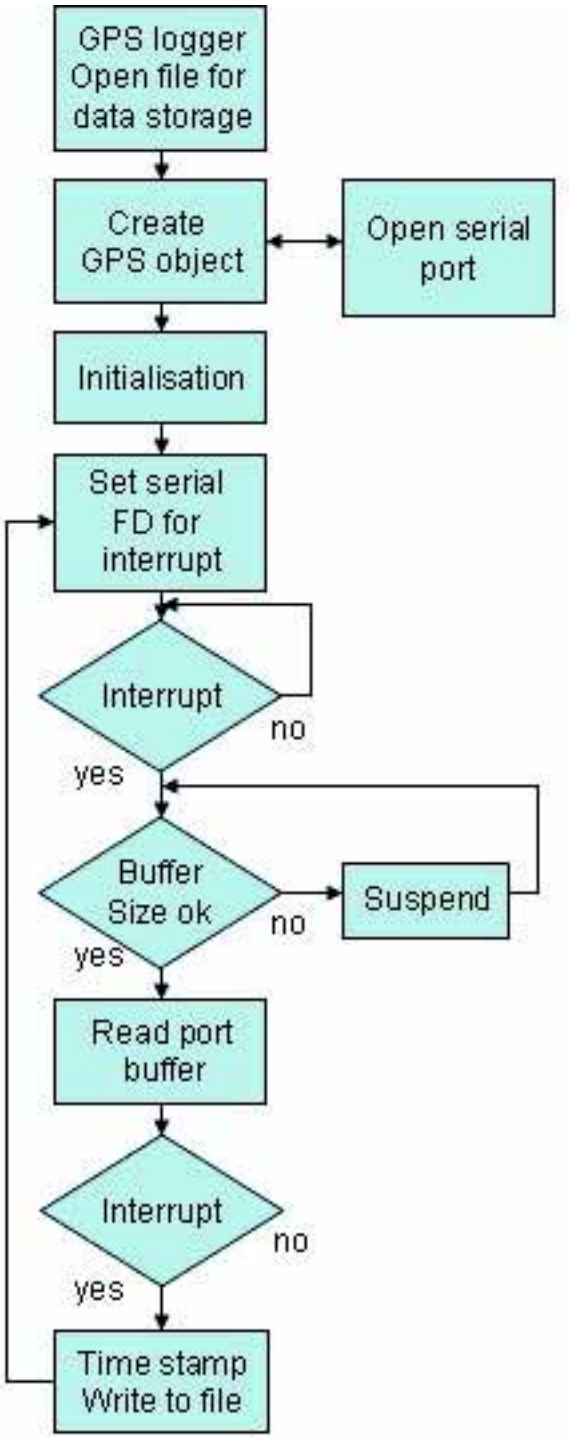


Figure 4.5: Flow diagram of the GPS-logger thread

# 5 IMU Error Modelling and Calibration

## 5.1 Deterministic IMU Errors

Calibration is essential to get correct measurements. This Section describes and uses calibration techniques for determining deterministic and stochastic IMU-errors. Information about the IMU error are used in designing the Kalman filter to integrate GPS and IMU.

### 5.1.1 Error Model

In order to take advantage of the sensor outputs, calibration of the sensor errors has to be done. Calibration is the process of comparing sensor outputs with known reference information and determine bias, scale factor, inertial axis misalignment, and other inertial sensor model parameters.

Consider the sensor error model (error terms of higher order than the first is disregarded)

$$
\begin{aligned}
\delta a_x^b &= \alpha_x + \alpha_{xx}a_x^b + \alpha_{xy}a_y^b + \alpha_{xz}a_z^b \\
\delta a_y^b &= \alpha_y + \alpha_{yx}a_x^b + \alpha_{yy}a_y^b + \alpha_{yz}a_z^b \\
\delta a_z^b &= \alpha_z + \alpha_{zx}a_x^b + \alpha_{zy}a_y^b + \alpha_{zz}a_z^b \\
\delta \omega_x^b &= \beta_x + \beta_{xx}\omega_x^b + \beta_{xy}\omega_y^b + \beta_{xz}\omega_z^b + \left(\beta_{xyx}a_x^b + \beta_{xyy}a_y^b + \beta_{xyz}a_z^b\right)\omega_y^b \\
&\quad + \left(\beta_{xzx}a_x^b + \beta_{xzy}a_y^b + \beta_{xzz}a_z^b\right)\omega_z^b \\
\delta \omega_y^b &= \beta_y + \beta_{yx}\omega_x^b + \beta_{yy}\omega_y^b + \beta_{yz}\omega_z^b + \left(\beta_{yxx}a_x^b + \beta_{yxy}a_y^b + \beta_{yxz}a_z^b\right)\omega_x^b \\
&\quad + \left(\beta_{yzx}a_x^b + \beta_{yzy}a_y^b + \beta_{yzz}a_z^b\right)\omega_z^b \\
\delta \omega_z^b &= \beta_z + \beta_{zx}\omega_x^b + \beta_{zy}\omega_y^b + \beta_{zz}\omega_z^b + \left(\beta_{zxx}a_x^b + \beta_{zxy}a_y^b + \beta_{zxz}a_z^b\right)\omega_x^b \\
&\quad + \left(\beta_{zyx}a_x^b + \beta_{zyy}a_y^b + \beta_{zyz}a_z^b\right)\omega_y^b
\end{aligned} \tag{5.1}
$$

Were the parameters in (5.1) is:

$\delta a_i^b$, $\delta \omega_i^b$, $(i = x, y, z)$ - accelerometer and gyroscope errors expressed in the body frame.

$\alpha_i$- accelerometer biases $\left[m/s^2\right]$

$\alpha_{ii}$- accelerometer scale factor [unit less]

$\alpha_{ij}$- accelerometer installation error $(i \neq j)$ [unit less]

$a_i^b$- accelerometer output in body frame coordinates $\left[m/s^2\right]$

$\beta_i$- gyro biases $[rad/s]$

$\beta_{ii}$- gyro scale factors [unit less]

$\beta_{ij}$- gyro installation error $(i \neq j)$ [unit less]

$\beta_{ijk}$- gyro drift depending on acceleration, flexure errors $\left[s^2/m\right]$

$\omega_i^b$- gyro output in body frame coordinates $[rad/s]$ In this report all installation errors and flexure errors will be disregarded.

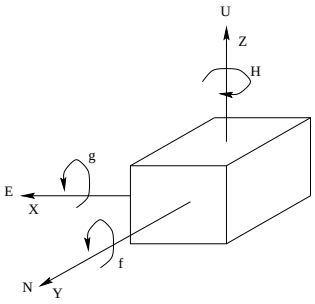


Figure 5.1: Initial IMU position for up-down calibration

### 5.1.2 Calibration Methods

#### 5.1.2.1 Accelerometer

Accelerometer calibration can be performed in a variety of ways. Accelerometers can be tested in vibration test, shock test, in a centrifuge or just measuring the gravity on turning table or on the dividing head in different angles [11]. Because cheap MEMS-sensors mostly are very temperature dependent and sometimes act like thermometers, it is common to calibrate at different temperatures.

To estimate accelerometer bias and scale factor an up-down test can be performed [16]. The method is a simple calibration procedure that uses the earth gravity to calibrate the accelerometers. The IMU is initially positioned so that the Z-axis of the IMU aligned with the local level frames U-axis, the Y-axis aligned with the N-axis and the X-axis aligned with the E-axis see figure 5.1. This enables the gravity component to affect only the accelerometer along the Z-axis of the IMU. If the IMU is then rotated 180° around the Y-axis a new measurement could be taken when the accelerometer along the Z-axis sense the negative gravity.

Let's consider an IMU with the $i$:th accelerometer aligned with the U-axis in a local level frame, the accelerometer output can then be formulated as

$$z^1\left(a_i^b\right) = \alpha_i + (\alpha_{ii} + 1)\, g$$

Where $g$ is the sensed gravity. Rotating the IMU 180° around perpendicular axis and making another measurement, gives the following output of the accelerometer would then be

$$z^2\left(a_i^b\right) = \alpha_i - (\alpha_{ii} - 1)\, g$$

By using the measurements above, the accelerometer scale factor and bias can be estimated as

$$\hat{\alpha}_i = \frac{z^1\left(a_i^b\right) + z^2\left(a_i^b\right)}{2} \qquad \hat{\alpha}_{ii} = \frac{z^2\left(a_i^b\right) + z^1\left(a_i^b\right) - 2g}{2g} \tag{5.2}$$

The same procedure is used to calibrate the three accelerometers in the IMU. The main drawback with this method is that the IMU must be perfectly aligned with the local frame, because the assumption is made that the gravity component only affects the axis the axis along the U-axis in the local frame. If the IMU is not perfectly aligned the gravity component will affect the other channels and therefor discredit the calibration.

#### 5.1.2.2 Gyroscope

The most common way to calibrate a gyroscope is via a rotation rate test on a rate table. Rotation rate tests are usually performed with the gyroscope inertial axis parallel to the table rotation axis oriented vertical, or sometimes parallel to the earth rotation vector. A sequence of different table rates is then performed and data from the gyroscope is logged. If scale factor asymmetry and nonlinearity is to be considered the sequence of table rates must contain positive and negative table rates. Even tough it is known that there are no asymmetry or nonlinearities in the scale factor a table rate sequence with positive and negative table rates can be used to get a better estimate of the scale factor. Assume the model equation, using the error model in (5.1).

$$\omega_{gj} = \beta_i + (\beta_{ii} + 1)(\omega_j + \omega_{ex}) \tag{5.3}$$

Where

$\omega_{gj}$ nominal gyro indicated angular rate at table angular rate $\omega_j$ [deg/h, rad/s].

$\omega_j$ average table angular rate for data segment $j$ [deg/h, rad/s].

$\omega_{ex}$ sensed component of earth rotation rate $\omega_e$ [deg/h, rad/s].

$\beta_i$ gyro bias [deg/h, rad/s].

$\beta_{ii}$ gyro scale factor

If gyro scale factor can be assumed linear and the bias can be assumed constant at a value $\beta_i$ from a earlier made drift test, then the scale factor can be determined from a single rotation rate. But if the bias can not be assumed constant from the time of the drift test, then the data from two rotation rates can be used to estimate the scale factor with the effect of bias removed.

$$\beta_{ii} = \frac{(\omega_{g1} - \omega_{g2}) - (\omega_1 - \omega_2)}{(\omega_1 - \omega_2)} \tag{5.4}$$

If complete revolutions are made at the rotation rate test, then the scale factor results are insensitive to misalignment angles between the gyroscope inertial axis and the rotation axis of the rate table, due to that the cosine of small angels is close to 1. The scale factor is also insensitive to misalignment between the earth rotation vector and the rotation axis of the rate table since the earth rotation component cancels out in the formula. Under the assumption that there are no scale factor or bias asymmetries and there are no nonlinearities, the most accurate calibration result is obtained if $\omega_1$ and $\omega_2$ is widely separated, even of opposite signs.

The gyro bias can be estimated from rate table measurements, (5.5), however drift rate test estimate of gyro bias has a much lower uncertainty. A *drift rate test* is a test where the gyro is at rest ($\omega_j = 0$) and data is collected during a long period of time hours, days and sometimes months. The estimated bias is then the mean value of the two sets of measurements compensated for the earth rotation rate.

$$\beta_i = \frac{\omega_{g1} + \omega_{g2}}{2} - (\beta_{ii} + 1)\frac{\omega_1 + \omega_2 + \omega_{ex}}{2} \tag{5.5}$$

### 5.1.3 Laboratory Calibration

The purpose of calibrating the IMU is to obtain estimates of the error parameters, that can be used to get a more accurate deterministic IMU error model for the Kalman filter. The calibration procedure was conducted in the gyro lab at FOI. Figure 5.2 shows a picture of the rate table on which the calibration was conducted. Unfortunately the rate tables control system was out of order. Instead a constant voltage was applied and the the rate was established by manually clocking a certain amount of revolutions. The IMU was mounted inside an aluminium cube, this enables the IMU to be rotated 90° in any direction.

Figure 5.2: Rate table at FOI gyro lab

#### Accelerometer bias and scale factor calibration

To extract the accelerometer bias and scale factor an up-down test was performed, see section 5.1.2.1. The IMU, mounted in the cube, was levelled so that the earth gravity component only affected the accelerometer to be calibrated. Data was collected during ten minutes then the IMU was rotated 180°, so that the accelerometer sensed the earth gravity in the opposite direction. In (5.2) the local gravity component is needed in order to estimate the scale factor and bias. The gravity component was evaluated for the Stockholm area at latitude $59°21'$ using the following model

$$g = 9.78049 + (1 + 0.0052884 \sin^2 \varphi - 0.0000059 \sin^2 2\varphi) \quad m/s^2$$

resulting in a gravity component of $9.8185\, m/s^2$. [15]

Figure 5.3 shows a data set for the calibration of the x accelerometer of the IMU. Equation (5.2) were used to estimate the bias and scale factor. By using

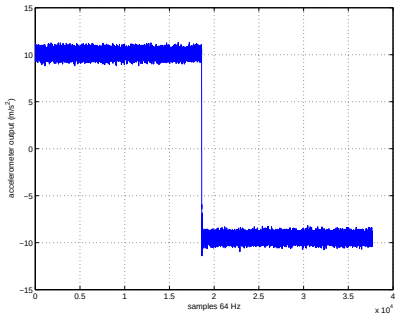


Figure 5.3: Data output for accelerometer.

the first 5 minutes of the data set as $z^1\left(a_x^b\right)$ and the last 5 minutes as $z^2\left(a_x^b\right)$. The accelerometer scale factors and biases has been estimated and are listed in table 5.1.

Table 5.1: Bias and Scale factor estimation for accelerometer x, y and z.

| Accelerometer | Bias $(m/s^2)$ | Scale factor (unit less) | $\hat{\alpha}_{ii}$ (%) |
|---|---|---|---|
| x | 0.2899 | $-4.7856 \cdot 10^{-4}$ | -0.005 |
| y | 0.2312 | $-0.0014$ | -0.14 |
| z | 0.1928 | $-0.0031$ | -0.31 |

According to the given technical specifications, Table 4.1, the IMU accelerometer scale factor accuracy should be $\leq 0.2$ %.

$$|\alpha_{xx}| = |\alpha_{yy}| = |\alpha_{zz}| \leq 0.002$$

However the calibration shows on a larger scale factor in the $z$-axis, see Table 5.1. One reason for this may be due to the calibration at the manufacturer. According to the manufacturer the IMU unit is not correctly pre-calibrated, see 4.1.1. Another reason for this can be that the scale factor is only estimated from one measurement, the earth gravitational component. In addition the used gravitational component may differ from the real value. In short the scale factor estimation for the accelerometers have many error sources.

The estimated accelerometer bias is

$$|\alpha_x| = |\alpha_y| = |\alpha_z| \leq 0.3\ m/s^2$$

see Table 5.1. This will result in deterministic bias of

$$0.3\ m/s^2 \Rightarrow \frac{0.3}{9.8185} \approx 0.03g = 30\ mg$$

According to Table 4.1, the residual bias error should be $\leq 5mg$. The previously mentioned incorrect pre-calibration may also be the reason for this discrepancy.

It is worth noting that the IMU seems to have a settling time. All data are collected after a settling time of 10 minutes.

#### Gyroscope bias and scale factor calibration

The rate table is controlled manually and open loop, which may result in errors. Because the computer controlling the rate table was out of order, the sequences for the different gyro channels $(x, y, z)$ may vary. Rotation rate test sequence and gyroscope output for gyroscope axes $x, y$ and $z$ can be seen in table 5.2, 5.3 and 5.4. All of the different rate sequences are run for at least one complete revolution. The higher rates are run approximately 15 minutes each. The associated errors, due to timing errors, to the measurements are $3 \cdot 10^{-5}$ $[rad/s]$ for the low rates and $2 \cdot 10^{-3}$ $[rad/s]$ for the highest rates.

Equation (5.4) was then used to estimate the scale factor for the gyroscopes. Measurements that are widely separated and of opposite sign could be used to achieve as accurate results as possible, see 5.1.2.2. The bias for the gyroscopes was estimated from a 50 minute long drift test, where the mean value of the drift rate test is the estimated bias. Table 5.5 shows the resulting estimates for the scale factor and biases. Comparing the estimated scale factor and bias, Table 5.5, with the given technical specifications in Table 4.1. One can see that the estimated bias for accelerometer $y$ and $z$ is larger than the specified residual bias $(0.5°/s)$, this can be due to the incorrect pre-calibration. That the scale factor for gyro $y$ is larger than the given error limit may be due

Table 5.2: Gyroscope rotation rate test sequence for gyro x

| table rate rad/s | gyro output rad/s |
|---|---|
| -0.0123 | -0.0136 |
| 0.0117 | 0.0102 |
| 0.0901 | 0.0860 |
| -0.0897 | -0.0938 |
| 0.2794 | 0.2760 |
| -0.2768 | -0.2798 |
| -0.4603 | -0.4618 |
| 0.4647 | 0.4608 |

Table 5.3: Gyroscope rotation rate test sequence for gyro y

| table rate rad/s | gyro output rad/s |
|---|---|
| 0.0117 | -0.0016 |
| -0.0121 | -0.2683 |
| 0.0860 | 0.0736 |
| -0.0858 | -0.1020 |
| 0.2741 | 0.2559 |
| -0.2713 | -0.2834 |
| -0.4603 | -0.4759 |
| 0.4658 | 0.4476 |

Table 5.4: Gyroscope rotation rate test for gyro z

| table rate rad/s | gyro output rad/s |
|---|---|
| -0.0113 | 0.0117 |
| 0.0114 | 0.0348 |
| 0.0877 | 0.1101 |
| -0.0868 | -0.0631 |
| -0.2750 | -0.2487 |
| 0.2770 | 0.3010 |
| 0.4671 | 0.4905 |
| -0.4630 | -0.4383 |

to the pre-calibration, but the estimated scale factor is associated with many error sources. The scale factor is assumed to be linear and symmetric, if this is not the case the estimated scale factor would be incorrect. The calibration procedure is also associated with errors because the computer controlling the rate table was out of order.

Table 5.5: Bias and scale factor estimates for gyro x, y and z.

| Gyro | Bias ($rad/s$) | Bias ($^\circ/s$) | Scale factor (unit less) | $\hat{\beta}_{ii}$ (%) |
|---|---|---|---|---|
| $x$ | 0.0003962 | 0.0227 | -0.0020 | -0.20 |
| $y$ | 0.0146681 | 0.8404 | -0.0042 | -0.42 |
| $z$ | 0.0195939 | 1.1226 | -0.0017 | -0.17 |

## 5.2 Stochastic IMU Errors

The Spectral analysis and Allan variance are used to determine the dominating stochastic IMU-errors. The Allan variance is investigated because it is easy to extract the error parameters and it can discern more error terms then the Power Spectral Density (PSD). The PSD and Allan variance is then compared to see that the Allan variance algorithm is properly implemented and how much the error parameters differ between the two methods.

### 5.2.1 Error Terms

There can be several error terms in a IMU, below the some of the error terms is listed and described for the acceleration and angular rate.

#### Quantisation Noise

Quantisation noise introduced into an analog signal, the error results from encoding the analog signal in digital form. Quantisation noise is caused by the small difference between the actual amplitudes of the sampled signal and the bit resolution of the analog-to-digital converter.

**White Noise** High frequency noise terms with correlation time much shorter than the sample time can contribute to the angle (velocity) random walk. Angular rate white noise can be a a major source of error that limits the performance of an attitude system.

**Bias Instability/Flicker Noise** Flicker noise is a low-frequency noise term that shows as bias fluctuations in the data, flickering. The origin of the noise is the electronics, or other components susceptible to random flickering.

**Random Walk** This is a random process of uncertain origin, possible a limiting case of an exponentially correlated noise with long correlation time.

### 5.2.2 Error Analysis

#### Power Spectral Density Analysis, PSD

The Power Spectral Density, PSD, of a time series of data describes how the power (or variance) is distributed with frequency. Mathematically the PSD is defined as the Fourier transform of the auto correlation sequence of the time series. Where the auto correlation is the expected value of the data multiplied by itself delayed.

The PSD is expressed in $units^2/Hz$ and it represents the "energy" in a time series $x(t)$ split into frequency components. A spike in the PSD represents a sinusoidal signal in the data . White noise is represented as a zero slope line parallel to the frequency axis in a PSD plot, white noise has constant power at all frequencies. Characteristic PSD log-log slopes of noise processes can be found in figure 5.4 for gyroscope angular rate data and Figure 5.5 for accelerometer data.

#### Allan Variance Analysis

The Allan variance is a statistical measure to characterise the stability of a time and frequency system over an interval of time. It is needed since the mathematical variance does not converge for all time and frequency system

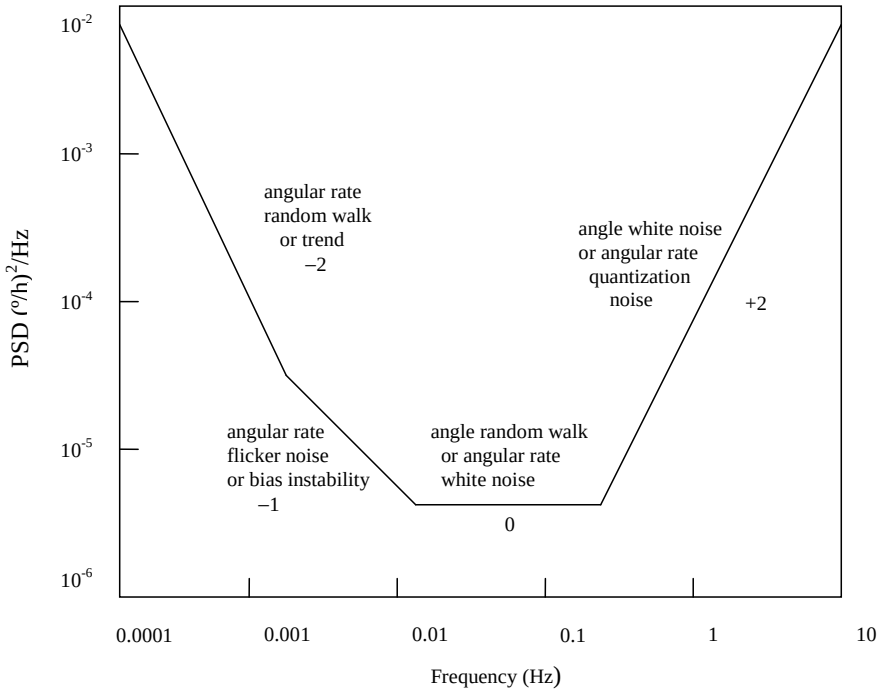


Figure 5.4: Typical slopes in log-log plot of one-sided PSD versus frequency for gyroscope angular rate data. Figure taken from [11] Figure 10.

noise processes. Retrieval of error parameters other than the white noise spectral density in a PSD plot is complex. In contrast, using the Allan variance, several other error parameters can be extracted fairly simple. The basic idea is to take a long data sequence and divide it into segments (clusters) based on an averaging time, $\tau$. Each segment is then averaged, the squared differences of the successive averaged segments added and divided by a rescaling factor. We now have a quantitative measure of how much the average value changes at that particular value of averaging time, $\tau$. Given a sequence with N elements $y_k$, $k = 0, 1, ..., N-1$, define for each $n = 1, 2, 3, ..., M \leq N/2$ a new sequence of averages of subsequences of the $y_k$:s with length $n$

$$x_j(n) = \frac{y_{nj} + y_{nj+1} + ... + y_{nj+n-1}}{n},\ j = 0, 1..., \left[\frac{N}{n}\right] - 1 \qquad (5.6)$$

If the sampling interval is $\Delta t$ , the time span within an averaged sequence of length $n$ is $\tau \triangleq n\Delta t$.

For a given $n$, the sequence $x_j(n)$ thus has $\left[\frac{N}{n}\right]$ elements when j runs from 0 to $\left[\frac{N}{n}\right] - 1$. From these, we can form the $\left[\frac{N}{n}\right] - 1$ differences $x_{j+1}(n) - x_j(n)$, with $j$ running from 0 to $\left[\frac{N}{n}\right] - 2$. The Allan variance, for the given subsequence length $n$, is now defined as half the average of these differences squared, i.e.

$$\sigma_a^2(\tau, N) \triangleq \frac{1}{2\left(\left[\frac{N}{n}\right] - 1\right)} \sum_{j=0}^{\left[\frac{N}{n}\right]-2} \left(x_{j+1}(n) - x_j(n)\right)^2 \qquad (5.7)$$

The square root of the Allan variance, i.e. the Allan standard deviation, is then plotted in a log-log diagram versus the averaging time $\tau$. Next a simple example is given to illustrate the principle.

**Example** Assume N=12 . Then n=1,2,3,4,5,6 lead to the following combinations :

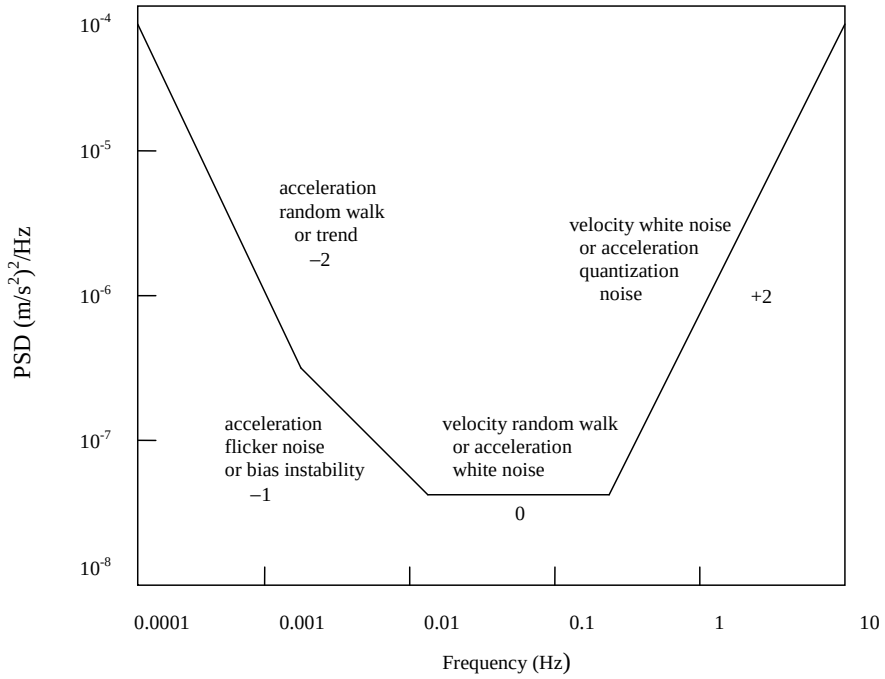


Figure 5.5: Typical slopes in log-log plot of one-sided PSD versus frequency for accelerometer acceleration data. Figure taken from [11] Figure 11.

$$
\begin{aligned}
n &= 1,\ \tau = \Delta t: \\
x_0(1) &= y_0, x_2(1) = y_2, \cdots, x_{11}(1) = y_{11}, \\
\sigma_a^2(\Delta t, 12) &= \frac{1}{2 \cdot 11} \sum_{j=0}^{10} (x_{j+1}(1) - x_j(1))^2 = \frac{1}{2 \cdot 11} \sum_{j=0}^{10} (y_{j+1} - y_j)^2.
\end{aligned}
$$

$$
\begin{aligned}
n &= 2, \tau = 2\Delta t: \\
x_0(2) &= \frac{y_0 + y_1}{2}, x_1(2) = \frac{y_2 + y_3}{2}, x_2(2) = \frac{y_4 + y_5}{2}, \\
x_3(2) &= \frac{y_6 + y_7}{2}, x_4(2) = \frac{y_8 + y_9}{2}, x_5(2) = \frac{y_{10} + y_{11}}{2}, \\
\sigma_a^2(2\Delta t, 12) &= \frac{1}{2 \cdot 5} \sum_{j=0}^{4} (x_{j+1}(2) - x_j(2))^2 \\
&= \frac{1}{2 \cdot 5} \sum_{j=0}^{4} \left[ \frac{y_{2j+2} + y_{2j+3}}{2} - \frac{y_{2j} + y_{2j+1}}{2} \right]^2.
\end{aligned}
$$

$$
\begin{aligned}
n &= 3, \tau = 3\Delta t: \\
x_0(3) &= \frac{y_0 + y_1 + y_2}{3}, x_1(3) = \frac{y_3 + y_4 + y_5}{3}, \\
x_2(3) &= \frac{y_6 + y_7 + y_8}{3}, x_3(3) = \frac{y_9 + y_{10} + y_{11}}{3}, \\
\sigma_a^2(3\Delta t, 12) &= \frac{1}{2 \cdot 3} \sum_{j=0}^{2} (x_{j+1}(3) - x_j(3))^2
\end{aligned}
$$

$$= \frac{1}{2\cdot 3}\sum_{j=0}^{2}\left[\frac{y_{3j+3}+y_{3j+4}+y_{3j+5}}{3} - \frac{y_{3j}+y_{3j+1}+y_{3j+2}}{3}\right]^2.$$

$$\begin{aligned}
n &= 4, \tau = 4\Delta t: \\
x_0(4) &= \frac{y_0+y_1+y_2+y_3}{4}, x_1(4) = \frac{y_4+y_5+y_6+y_7}{4}, \\
x_2(4) &= \frac{y_8+y_9+y_{10}+y_{11}}{4}, \\
\sigma_a^2(4\Delta t, 12) &= \frac{1}{2\cdot 2}\sum_{j=0}^{1}(x_{j+1}(4)-x_j(4))^2 \\
&= \frac{1}{2\cdot 2}\sum_{j=0}^{1}\left[\frac{y_{4j+4}+y_{4j+5}+y_{4j+6}+y_{4j+7}}{4} - \frac{y_{4j}+y_{4j+1}+y_{4j+2}+y_{4j+3}}{4}\right]^2.
\end{aligned}$$

$$\begin{aligned}
n &= 5, \tau = 5\Delta t: \\
x_0(5) &= \frac{y_0+y_1+y_2+y_3+y_4}{5}, x_1(5) = \frac{y_5+y_6+y_7+y_8+y_9}{5}, \\
\sigma_a^2(5\Delta t, 12) &= \frac{1}{2\cdot 1}(x_1(5)-x_0(5))^2 \\
&= \frac{1}{2\cdot 1}\left[\frac{y_5+y_6+y_7+y_8+y_9}{5} - \frac{y_0+y_1+y_2+y_3+y_4}{5}\right]^2.
\end{aligned}$$

$$\begin{aligned}
n &= 6, \tau = 6\Delta t: \\
x_0(6) &= \frac{y_0+y_1+y_2+y_3+y_4+y_5}{6}, x_1(6) = \frac{y_6+y_7+y_8+y_9+y_{10}+y_{11}}{6}, \\
\sigma_a^2(6\Delta t, 12) &= \frac{1}{2\cdot 1}(x_1(6)-x_0(6))^2 \\
&= \frac{1}{2\cdot 1}\left[\frac{y_6+y_7+y_8+y_9+y_{10}+y_{11}}{6} - \frac{y_0+y_1+y_2+y_3+y_4+y_5}{6}\right]^2.
\end{aligned}$$

For n=5 it is not possible to use all the data points due to the fact that the integer part $\left[\frac{N}{n}\right]$ of $\left[\frac{N}{n}\right]$ is used. In order to demonstrate the quality of estimation of the true Allan standard deviation, we define its relative error as

$$\delta_{AV}(\tau, N) \triangleq \frac{\sigma_a(\tau, N) - \sigma_a(\tau, \infty)}{\sigma_a(\tau, \infty)}. \tag{5.8}$$

This is justified by the fact that $\sigma_a(\tau, \infty)$ is based upon an infinite number of independent data and can thus be regarded as the standard deviation's "true value", as it has zero variance. A lengthy but straightforward calculation shows that the relative error $\sigma_a(\tau, N)$ has the variance

$$Var(\delta_{AV}(\tau, N)) = \frac{1}{2\left(\frac{N}{\tau}\Delta t - 1\right)}. \tag{5.9}$$

From this expression it is clear that the relative error increases with the subsequence length $\tau$, which is natural as the number of subsequences decreases with increasing $\tau$. More about this in [4] and in [5]. Figure 5.6 shows the Allan standard deviation as function of $\tau$ for gyroscope angle velocity noise in a log-log plot, and figure 5.7 for accelerometer acceleration noise. For short averaging times $\tau$, the Allan variance is dominated by quantization noise. There is a direct correlation between the standard deviation of the output versus time

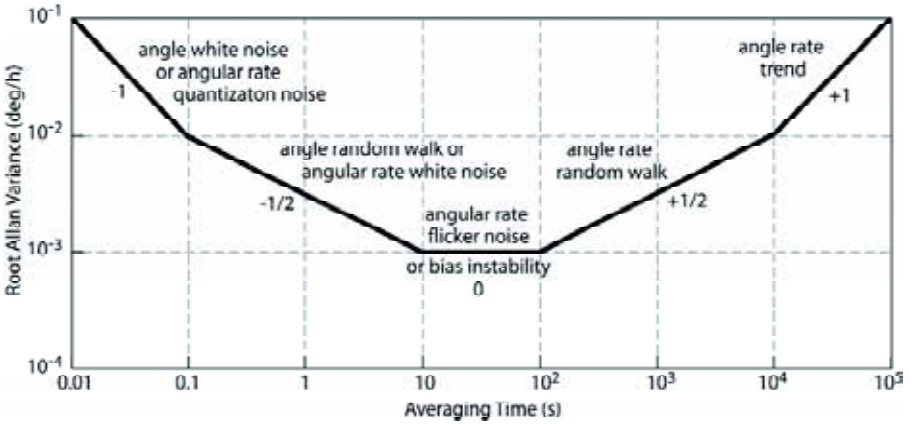


Figure 5.6: Typical slopes in log-log plot of square root of Allan variance versus averaging time for gyroscope angular rate. Figure taken from [11] Figure 12.

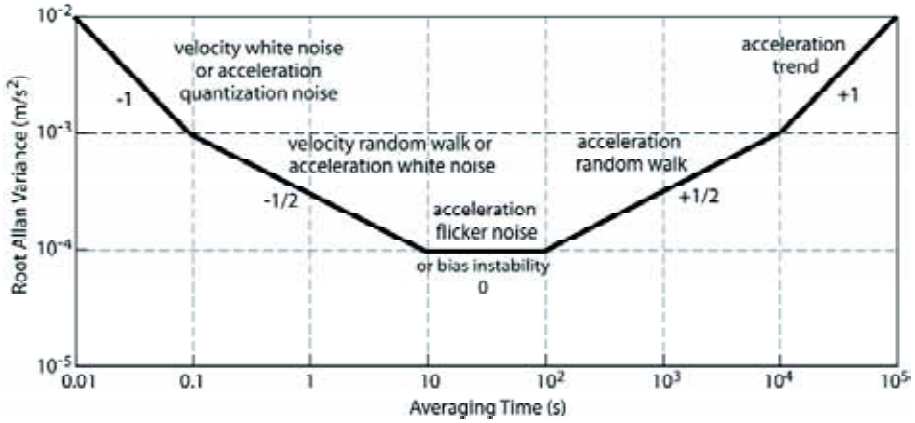


Figure 5.7: Typical slopes in log-log plot of square root of Allan variance versus averaging time for accelerometer acceleration data. Figure taken from [11] Figure 13.

with the slope of the Allan variance at small $\tau$. This is called angle random walk (ARW) for gyroscopes and velocity random walk (VRW) for accelerometers. As averages are taken over longer and longer times the variance decreases. When the averaging time increases even more, the Allan variance starts to increase, due to long term variations in the bias. This is called rate random walk (RRW) for gyroscopes and acceleration random walk for accelerometers

### 5.2.3 Laboratory Tests

The data used to process the PSD and Allan variance, is data from a 50 minute long drift test. The Allan variance need a long data set to discern all error terms, data sets up to 2 hours is not unusual.

PSD

Figure 5.8 shows a log log plot of the PSD of gyro x of the IMU. Due to bunching of the high frequency data points, it is difficult to identify the noise terms and the parameters associated with them. To be able to identify the noise terms the frequency averaging technique [3] is used to reduce the number of data points. Figure 5.9, 5.10 and 5.11 shows the PSD result, with the frequency averaging technique, for gyro x, y and z. From figure 5.9 and 5.10 the slopes of the the curve include -2, -1, 0, and +2, this indicates that the gyro data contains angular rate random walk, angular rate flicker noise, angle random walk and angular rate quantisation noise. In figure 5.11 it is hard to determine if the gyro has any influence of angular rate random walk due to the lack of measuring points. Figure 5.12, 5.13 and 5.14 shows the PSD result, with

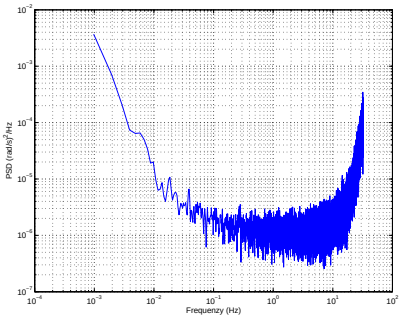


Figure 5.8: PSD results of gyro x

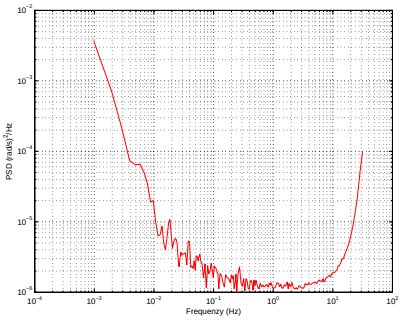


Figure 5.9: PSD result for gyro x with frequency averaging technique

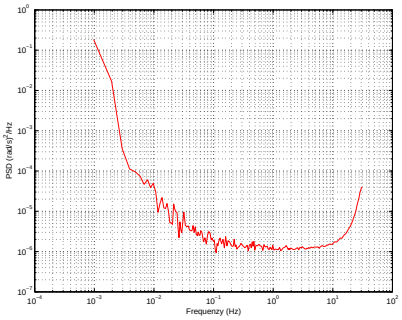


Figure 5.10: PSD result for gyro y with frequency averaging technique

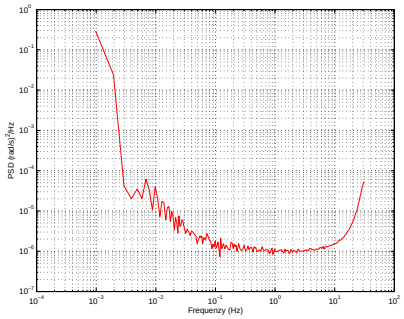


Figure 5.11: PSD result for gyro z with frequency averaging technique

the frequency averaging technique, for accelerometer x, y and z. From figure 5.12 and 5.13 the slopes of the curve include -2, -1, 0, and +2, this indicates that the accelerometer data contains acceleration random walk, acceleration flicker noise, velocity random walk and acceleration quantisation noise. The PSD of the $z$ accelerometer , in Figure 5.14, do not have the inclination of -1, this means that the $z$ accelerometer lacks the acceleration flicker noise term.

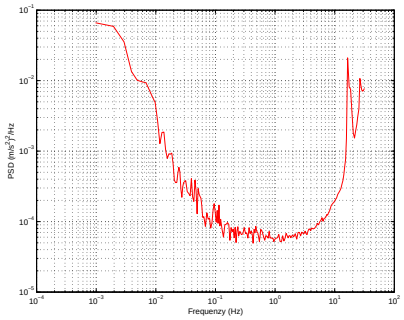


Figure 5.12: PSD result for accelerometer x with frequency averaging technique

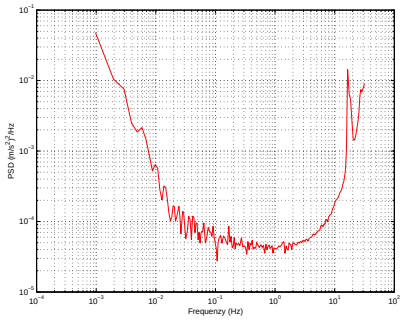


Figure 5.13: PSD result for accelerometer y with frequency averaging technique

Parameter acquisition of noise terms from a PSD plot is complex, beside the angular rate and acceleration white noise. Table 5.6 shows the estimated white noise for the accelerometers and gyros. Converting the angular white noise into units of $^\circ/\sqrt{h}$ using (5.10), and the acceleration white noise into units of $m/s/\sqrt{h}$ with (5.11) if the values are from a one-sided PSD.

$$\left[^\circ/\sqrt{h}\right] = \frac{1}{60} \cdot \frac{1}{\sqrt{2}} \left(\frac{180}{\pi} \cdot 3600\right) \left[\frac{rad/s}{Hz}\right] \tag{5.10}$$

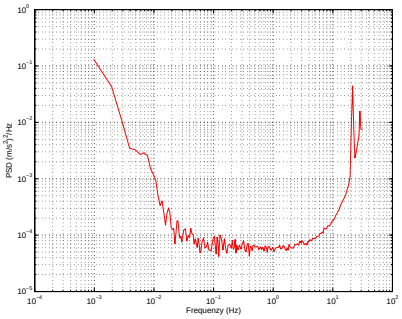


Figure 5.14: PSD result for accelerometer z with frequency averaging technique

Table 5.6: PSD estimation results for accelerometers and gyros

| Noise term | $x$ axis | $y$ axis | $z$ axis |
|---|---|---|---|
| Angular rate white noise $\left[(rad/s)/\sqrt{Hz}\right]$ | $1.1 \cdot 10^{-3}$ | $1.1 \cdot 10^{-3}$ | $1 \cdot 10^{-4}$ |
| Acceleration white noise $\left[(m/s^2)/\sqrt{Hz}\right]$ | $7.9 \cdot 10^{-3}$ | $6.8 \cdot 10^{-3}$ | $9.4 \cdot 10^{-3}$ |

$$\left[m/s/\sqrt{h}\right] = 60 \cdot \frac{1}{\sqrt{2}} \left[\frac{m}{s^2}/\sqrt{Hz}\right] \tag{5.11}$$

Table 5.7 shows the estimated white noise from the PSD plots with converted units. Analog Devices states an angular random walk of 6 $\left(^\circ/\sqrt{h}\right)$

Table 5.7: PSD estimation result for accelerometers and gyros

| Noise term | $x$ axis | $y$ axis | $z$ axis |
|---|---|---|---|
| Angular rate white noise $\left[^\circ/\sqrt{h}\right]$ | 2.71 | 2.68 | 2.42 |
| Acceleration white noise $\left[m/s/\sqrt{h}\right]$ | 0.33 | 0.29 | 0.40 |

at $25°C$ for the ADXRS300 gyros, which are used in the MICRO ISU BP3010 IMU. If we compare this to Table 5.7, we can see that the PSD result for the white noise level lies well within the limits of the manufacturer. The given accelerometer power spectral density is 200 $\left[\mu g/s/\sqrt{Hz}\right] = 200\mu \cdot 9.81 \cdot \left[m/s^2/\sqrt{Hz}\right]$ by using (5.11) to convert this specification into velocity random walk 0.1177 $\left[m/s/\sqrt{h}\right]$. The maximum accelerometer PSD is also given as 1000 $\left[\mu g/s/\sqrt{Hz}\right] = 1000\mu \cdot 9.81 \cdot \left[m/s^2/\sqrt{Hz}\right]$ and converted to maximum velocity random walk 0.4166 $\left[m/s/\sqrt{h}\right]$. The PSD measurement result of the white noise level for the accelerometers also lies below the maximum noise level but a little higher then the typical value.

The PSD result indicates that there are several noise terms in addition to the angular rate and acceleration white noise.

### Allan Variance

The Allan variance in section 5.2.2 is another tool to analyse the noise terms and extract the noise parameters. In difference to the PSD the Allan variance can discern angular rate (acceleration) random walk as well as angular rate (acceleration) trend, which in the PSD case is perceived as one noise term. The difference can be seen by comparing Figure 5.4 and 5.5 with Figure 5.6

and 5.7. Figure 5.15, 5.16 and 5.17 shows log-log plots of the square root Allan variance for the gyros. The plots also contains the square root Allan variance uncertainty bounds according to (5.9) described in section 5.2.2. The log-

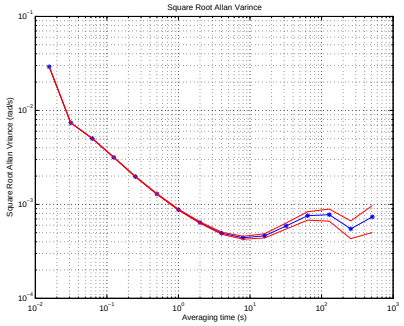


Figure 5.15: Estimated square-root Allan variance with error limits for gyro x.

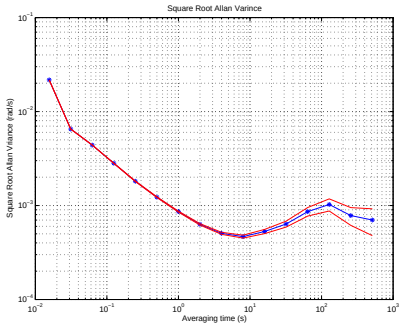


Figure 5.16: Estimated square-root Allan variance with error limits for gyro y.

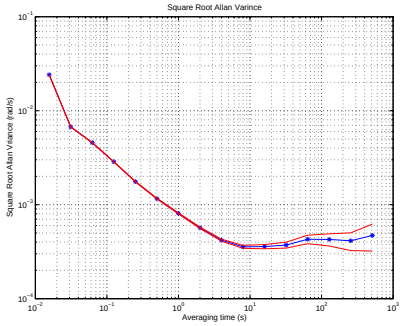


Figure 5.17: Estimated square-root Allan variance with error limits for gyro z.

log plots of the square-root Allan variance in Figure 5.15 and 5.16 shows the presence of angular rate white noise (slope $-1/2$), angular rate flicker noise (slope 0) and angular rate random walk (slope $+1/2$). While the log-log plot of the square-root Allan variance of the $z$-gyro in Figure 5.17, only shows the presents of angular rate white noise (slope $-1/2$) and angular rate flicker noise (slope 0). This result is consistent with the result from the PSD plots. The $-2$ slope at short averaging times is some unknown error of unknown origin, this strange behaviour can also be seen in the PSD plots for high frequencies. Figure 5.18, 5.19 and 5.20 shows the log-log square-root Allan variance for

accelerometer $x$, $y$ and $z$ respectively. Figure 5.18 and 5.19 shows the presence of acceleration quantisation noise (slope $-1$), acceleration white noise (slope $-1/2$), acceleration flicker noise (slope 0) and acceleration random walk (slope $1/2$). While the the Allan variance of accelerometer $z$ in Figure 5.20 do not have any acceleration flicker noise.

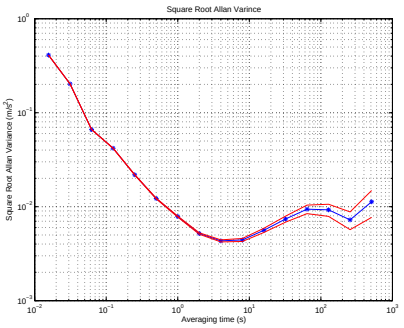


Figure 5.18: Estimated square-root Allan variance with error limits for accelerometer x.

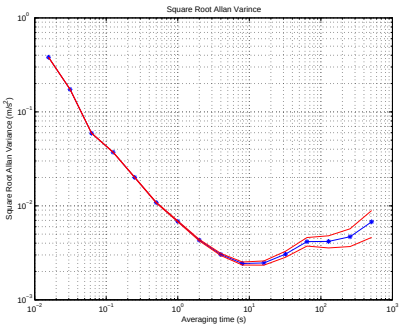


Figure 5.19: Estimated square-root Allan variance with error limits for accelerometer y.

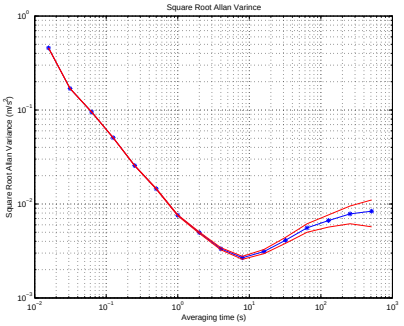


Figure 5.20: Estimated square-root Allan variance with error limits for accelerometer z.

To extract the different noise parameters a straight line is fitted to the plot and the noise coefficient can be read out [12]. For example, if the white noise coefficient should be obtained, a straight line with slope $-1/2$ would be fitted to the log-log plot of the square-root Allan variance. The white noise coefficient is obtained by reading the slope line at $\tau = 1$. Below the relations between the square root Allan variance and the PSD for the different noise parameters are listed. Where $\sigma$ is the square-root Allan variance and $\tau$ is the averaging time.

- Quantization Noise.

$$\sigma(\tau) = Q_z \cdot \frac{\sqrt{3}}{\tau} \tag{5.12}$$

  Where $Q_z$ is the quantization noise coefficient.

- Angular rate (Acceleration) white noise.

$$\sigma(\tau) = \frac{Q}{\sqrt{\tau}} \tag{5.13}$$

  Where $Q$ is the white noise coefficient.

- Angular rate (Acceleration) flicker noise

$$\sigma(\tau) = \sqrt{\frac{2 \cdot \ln 2}{\pi}} B \tag{5.14}$$

  Where $B$ is the flicker noise coefficient.

- Angular rate (Acceleration) random walk.

$$\sigma(\tau) = K\sqrt{\frac{\tau}{3}} \tag{5.15}$$

  Where $K$ is the random walk coefficient.

- Angular rate (Acceleration) trend.

$$\sigma(\tau) = R\frac{\tau}{\sqrt{2}} \tag{5.16}$$

  Where $R$ is the trend coefficient.

The realtive error in the Allan variance is calculated using 5.9. Table 5.8 shows the estimated noise coefficients for the gyros and Table 5.9 shows the estimated noise coefficients for the accelerometers. $\surd$ means that the sensor lacks the error.

Table 5.8: Identified Noise Coefficients for the gyros, using Allan variance.

| | $Q_z$[rad] | $Q$ $[rad/\sqrt{s}]$ | $B$ $[(rad/s]$ | $K$ $[rad/s/\sqrt{s}]$ | $R$ $\left[rad/s^2\right]$ |
|---|---|---|---|---|---|
| $x$ | $\surd$ | $(8.8 \pm 0.3) \cdot 10^{-4}$ | $(4.7 \pm 0.2) \cdot 10^{-4}$ | $(1.8 \pm 0.2) \cdot 10^{-4}$ | $\surd$ |
| $y$ | $\surd$ | $(8.7 \pm 0.3) \cdot 10^{-4}$ | $(4.7 \pm 0.2) \cdot 10^{-4}$ | $(1.9 \pm 0.2) \cdot 10^{-4}$ | $\surd$ |
| $z$ | $\surd$ | $(8.1 \pm 0.3) \cdot 10^{-4}$ | $(3.6 \pm 0.2) \cdot 10^{-4}$ | $\surd$ | $\surd$ |

Table 5.9: Identified Noise Coefficients for the accelerometers, using Allan variance

| | $Q_z$ $[m/s]$ | $Q$ $[m/s/\sqrt{s}]$ | $B$ $\left[m/s^2\right]$ | $K$ $\left[m/s^2/\sqrt{s}\right]$ | $R$ $\left[m/s^3\right]$ |
|---|---|---|---|---|---|
| $x$ | $(36.9 \pm 0.5) \cdot 10^{-4}$ | $(78.4 \pm 2.8) \cdot 10^{-4}$ | $(43.8 \pm 2.3 \cdot 10^{-4}$ | $(23.2 \pm 2.4) \cdot 10^{-4}$ | $\surd$ |
| $y$ | $(30.8 \pm 0.4) \cdot 10^{-4}$ | $(61.0 \pm 2.2) \cdot 10^{-4}$ | $(24.5 \pm 1.3) \cdot 10^{-4}$ | $(9.8 \pm 1.0) \cdot 10^{-4}$ | $\surd$ |
| $z$ | $(40.7 \pm 0.5) \cdot 10^{-4}$ | $(69.7 \pm 2.5) \cdot 10^{-4}$ | $\surd$ | $(13.4 \pm 1.4) \cdot 10^{-4}$ | $\surd$ |

### 5.2.4 Comparison of PSD and Allan Variance Extracted White Noise Coefficient

To be able to compare the extracted white noise coefficient result from the Allan variance with the result from the PSD the former is converted to $\left[^\circ/\sqrt{h}\right]$ for the gyros and $\left[m/s/\sqrt{h}\right]$ for the accelerometer error coefficients. Table 5.10 shows the comparison between the PSD and Allan extracted white noise coefficient. The white noise coefficients is very similar in the PSD extraction and the Allan variance extraction. The difference can be due to read out errors in the PSD plot or a small error due to the frequency averaging in the PSD plots, or a read out error in the Allan variance plots.

Table 5.10: Comparison between PSD extracted white noise coefficient and Allan variance extracted white noise coefficient.

| | Gyro PSD $\left[^\circ/\sqrt{h}\right]$ | Gyro Allan $\left[^\circ/\sqrt{h}\right]$ | Accl. PSD $\left[m/s/\sqrt{h}\right]$ | Accl. Allan $\left[m/s/\sqrt{h}\right]$ |
|---|---|---|---|---|
| $x$ | 2.71 | $3.02 \pm 0.1$ | 0.33 | $0.47 \pm 0.02$ |
| $y$ | 2.68 | $3.00 \pm 0.1$ | 0.29 | $0.37 \pm 0.01$ |
| $z$ | 2.42 | $2.8 \pm 0.1$ | 0.40 | $0.42 \pm 0.02$ |

### 5.2.5 MICRO-ISU BP3010 Performance

To get an idea of how the performance of the MICRO-ISU BP3010 is the MICRO-ISU BP3010, which is of consumer grade, is compared with three other IMU:s with different quality:

- Navigation grade IMU: The Honeywell CIMU
- Tactical grade IMU: The Honeywell HG1700
- Consumer grade MEMS based IMU: The Systron Donner MotionPack II-3g

The evaluation of these IMU:s is performed in [12] from a two hour data set. Table shows the noise coefficients for the different IMU:s

Table 5.11: Comparison of noise coefficients of the gyros for different IMU quality

| | $Q_z$ $[^\circ]$ | $Q$ $\left[^\circ/\sqrt{h}\right]$ | $B$ $[^\circ/h]$ | $K$ $\left[^\circ/h/\sqrt{h}\right]$ | $R$ $\left[^\circ/h^2\right]$ |
|---|---|---|---|---|---|
| CIMU | 0.00014 | 0.0015 | $\surd$ | $\surd$ | $\surd$ |
| HG1700 | 0.00035 | 0.0883 | $\surd$ | $\surd$ | $\surd$ |
| MP II | $\surd$ | 0.4891 | 16.79 | $\surd$ | $\surd$ |
| BP3010 | $\surd$ | 3.0252 | 96.94 | 222.77 | $\surd$ |

Table 5.12: Comparison of noise coefficients of the accelerometers for different IMU quality

| | $Q_z$ $[m/h]$ | $Q$ $\left[m/s/\sqrt{h}\right]$ | $B$ $[m/s/h]$ | $K$ $\left[m/s/h/\sqrt{h}\right]$ | $R$ $\left[m/s/h^2\right]$ |
|---|---|---|---|---|---|
| CIMU | 1.6801 | $\surd$ | $\surd$ | $\surd$ | 2.6364 |
| HG1700 | 2.1988 | $\surd$ | $\surd$ | 1.1572 | $\surd$ |
| MP II | $\surd$ | 0.01612 | 4.36 | $\surd$ | $\surd$ |
| BP3010 | 13.284 | 0.4704 | 15.768 | 501.12 | $\surd$ |

One can see that the BP3010 has much higher noise coefficients then the other IMU:s

# 6 Experiment

This chapter describes the two different experiments. A high dynamic test in a roller coaster and a low dynamic test in a car.

## 6.1 High Dynamic

The high dynamic test were conducted in October 2004, in a roller coaster called "vilda musen" at Gröna lund in Stockholm. Some of the reasons for conducting the experiment in a roller coaster is because of the:

- High dynamic with three dimensional motion
- Good repeatability
- Three dimensional rotation and acceleration
- Access to AutoCad data of the roller coaster

The size of the roller coaster construction is:

- Width ~ 100 $[m]$
- Depth ~ 40 $[m]$
- Height ~ 60 $[m]$

and the track width is 0.8 $[m]$ with a total track length of 480 $[m]$. The maximum pitch and roll angle is 50° and 81° respectively. The maximum speed depends on the surrounding temperature, humidity and load of the wagon resulting in a velocity of about 60 $[km/h]$ and a maximum acceleration of about $3 - 4g$. The experimental location also has its limitations, during a run there are vibrations and swaying in the construction produced by the other wagons and the chain dragging the wagons up the first hill. There are mainly two locations on the course where the wagon goes under a roof and between in narrow passage. In these locations satellite outage may occur. Due to the metal construction there is a high risk of multipath.

Figure 6.1 shows the reference trajectory of the roller coaster. The reference data of the roller coaster is provided by Stengel AG in München. In addition to the position coordinates for the roller coaster also yaw, roll and pitch angles are provided. A total of 11 laps were made during the experiment logging data from the navigation sensors and the reference GPS. The test procedure started with an 5 minutes initialization at the start point, see Figure 6.1, to obtain a good initial attitude and position from the reference GPS. A lap takes about 60 seconds and ends at the stopping point also marked in Figure 6.1. The GPS antennas were mounted as in Figure 4.4.
However after having analyzed the data it was clear that there was not enough number of satellites available for a sufficient long time for a Kalman filter to converge and to be able to estimate the IMU errors. For example, after just

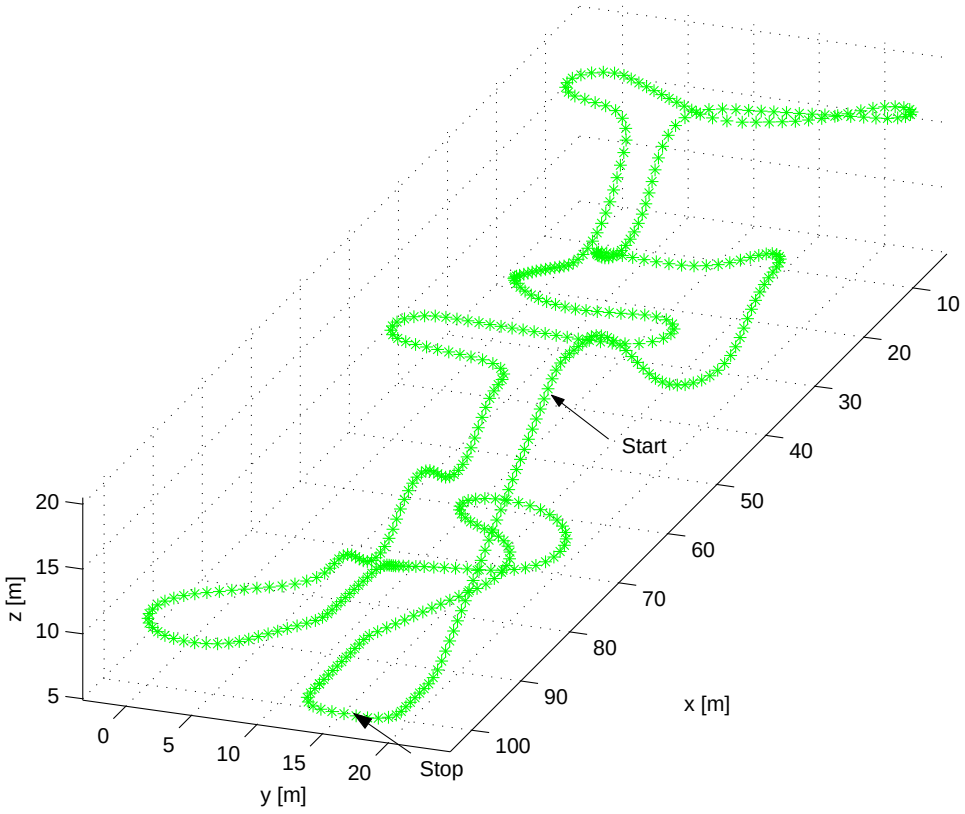


Figure 6.1: Reference trajectory of the roller coaster. The start position is marked.

10 seconds after start the number of satellites dropped to 20% of what was available at that time.

During the experiments a GPS software receiver NORDNAV R30 was used to record RF data during some of the laps of the experiment. The reason for this was to be able to postprocess the data and tune the GPS receiver parameters making more satellites available. However by increasing the GPS receiver tracking bandwidth, the measurement noise in the pseudo distances also increases. More satellites was achieved, but the price for this was increased measurement noise that led to a severe degraded position solution.

Also the reference GPS receiver (Javad HD-2) was very sensitive to vibrations and high dynamics making it difficult to analyze the filter performance.

So the initial high dynamic test's resulted in many important experiences where the most important are:

- The reference system in position and attitude has to be high performing and robust to high dynamic and satellite outages.

- Maximize the number of satellites during the experiments by simulating the satellite availability. Higher antenna placement. The rear operator was limiting the sky view.

To be able to test and tune the Kalman filter parameters new experiments was conducted by using a Volvo 945 on a test track in Ursvik.

## 6.2 Low Dynamic

The 5 minutes data set used to validate the filters was collected at FOI:s establishment in Ursvik the 20th December 2004. The data were collected with the navigation equipment explained in 4. The navigation equipment was mounted in the trunk of a Volvo 945, the Superstar II antenna and the GPS reference antennas were mounted on a pole as in the high dynamic case, see Figure 4.4. The pole were strapped to the roof of the car enabling the reference GPS to measure the pitch and yaw angles of the vehicle. To optimize satellite availability the experiment was conducted when the number of satellites peaked. In total five laps were made logging data from the sensors. The sensors were exposed to large temperature fluctuations, due to opening of doors of the test vehicle. The temperature difference between the inside and outside of the test vehicle were large because of the heater in the car and the cold weather outside. The test track can be seen in Figure 6.2, the red line represents the reference GPS position for all laps made during the experiment, the car was moving clock wise starting just before label $A$. The green blocks in the figure represents buildings.

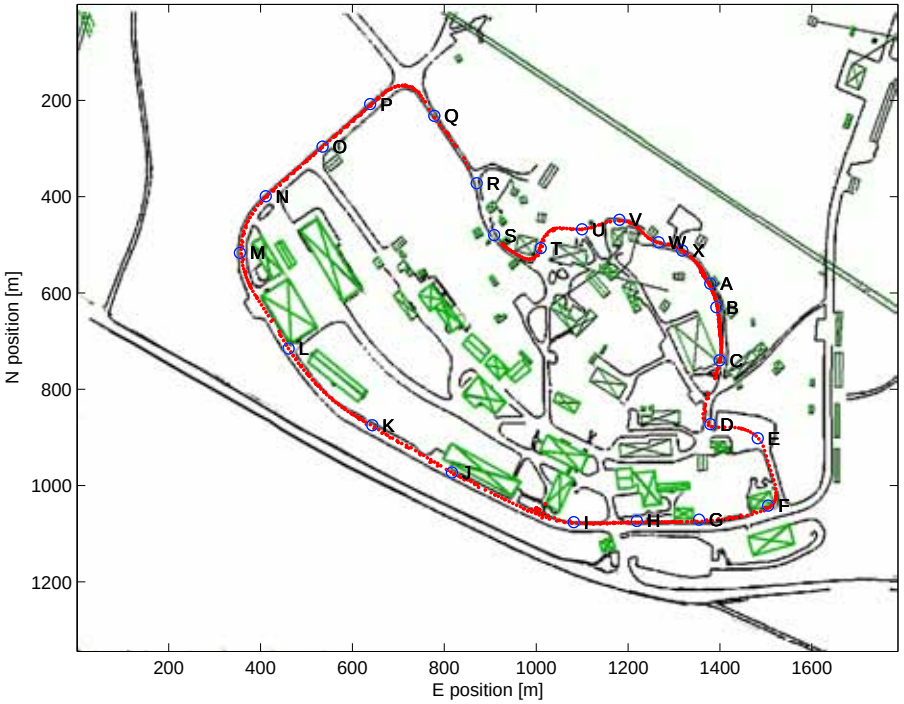


Figure 6.2: GPS reference trajectory expressed in a local frame projected on an Ursvik map.

### 6.2.1 Environment. Satellite Constellation, availability and Visibility

Table 6.1 describes the entire car run in time segments determined by carefully chosen positions marked by letter labels, Figure 6.2. Each row in the table corresponds to a segments with its time interval, so as to more easy compare two dimensional $x - y$ plots with time plots. It also contains the number of used satellites, VDOP, HDOP associated with the Superstar II GPS receiver. And a column that in short describes the environment and how the vehicle is moving. The letters $A - X$ labels to mark interesting events and to aid the

comparison between two dimensional $x-y$ plots with time plots. The events corresponding to these letters are described in Table 6.1 and can be seen in Figure 6.2.

Table 6.1: Summary of parameters for the used data set.

| Position | Time (s) | Nr Sv | VDOP | HDOP | Description/Environment |
|---|---|---|---|---|---|
| Start-A | $0-31$ | 8 | 1.2 | 1 | No obstruction. Starts moving at A. |
| A-B | $31-35$ | 4 | 12.2 | 20 | No obstruction. Down hill. |
| B-C | $35-46$ | $4-6$ | $2-4$ | $1.5-4$ | Building on west side. Down hill. |
| C-D | $46-56$ | $4-6$ | $2-4$ | $1.5-2$ | Fairly open, some trees. Down hill. |
| D-E | $56-64$ | 5 | 2 | 2 | No obstruction. Level. |
| E-F | $64-73$ | $2-5$ | $2-4.2$ | $2-4$ | No obstruction. Down hill. |
| F-G | $73-83$ | $4-6$ | $2-4.2$ | $1.5-4$ | Building on south side. Level. |
| G-H | $83-92$ | $5-6$ | $2-2.7$ | $1.5-2$ | Building on north side. Level. |
| H-I | $92-101$ | $5-6$ | 2 | 1.5 | Buildings on north-east and north-west side. Level. |
| I-J | $101-115$ | $2-5$ | $2-9.5$ | $2-14$ | Building on north side. Level. |
| J-K | $115-126$ | $4-7$ | $1.7-4$ | $1.5-4$ | Building on north side. Level. |
| K-L | $126-139$ | $5-7$ | 1.7 | $1.5-2$ | Building on north side. Level. |
| L-M | $139-150$ | $3-5$ | $2-5$ | $2.5-5$ | Building on north-east side. Level. |
| M-N | $150-155$ | 5 | 2 | 2.5 | Right turn. Building on east side. Level. |
| N-O | $155-165$ | $4-5$ | 2 | 2.5 | No obstruction . Level. |
| O-P | $165-174$ | $5-7$ | 2 | $1.5-2.5$ | Building on south-east side at O. Level. |
| P-Q | $174-186$ | $3-7$ | $2-5$ | $2-17$ | Sharp right turn. Forest begins at Q. Level. |
| Q-R | $186-196$ | $4-5$ | $2-9$ | $2-5$ | Forest. Up hill. |
| R-S | $196-204$ | $4-7$ | $2-5$ | $2-5$ | Forest, buildings at north and south side. Up hill. |
| S-T | $204-215$ | $5-7$ | $2-4.5$ | $2-9$ | Left turn. Building on north side. Up hill. |
| T-U | $215-223$ | $2-6$ | $2-9$ | $2-6$ | Right turn. Building on east and west side. Up hill. |
| U-V | $223-228$ | $4-7$ | $2-7$ | $2-21$ | Fairly open. Up hill. |
| V-W | $228-237$ | $4-6$ | $2.5-7$ | $2-21$ | No obstruction. Up and down hill. |
| W-X | $237-242$ | $5-7$ | $1.5-2$ | 1.5 | No obstruction. Up hill. |
| X-Stop | $242-287$ | $6-9$ | 1.5 | 1 | No obstruction. Stationary. |

The satellite visibility for the Superstar II GPS receiver during the run can be seen in Figure 6.3. The $y$-axis shows the satellite vehicle number (Sv) and the $x$-axis is the elapsed time. Thereby the solid line shows when a particular satellite has been visible to the Superstar II GPS receiver. Figure 6.4 is a skyplot showing the satellite constellation during the run. The track of the satellite vehicles that are visible are plotted here. The circles in the grid is the elevation angle with zenith ($90°$) in the centre and the azimuth angle with north at $0°$. Figures 6.5, 6.6 and 6.7 represents the VDOP, HDOP and the number of used satellites for the Superstar II, respectively. It should be noted that these plots are for the Superstar II GPS receiver but it is likely that the reference GPS system lso has about the same number of satellites.

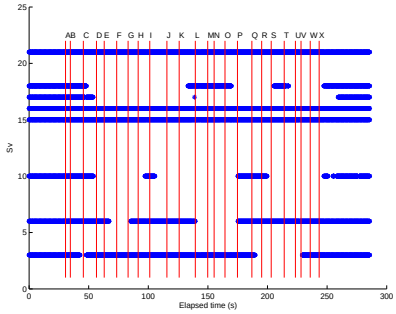


Figure 6.3: Satellite visibility for the entire run of about 5 minutes. For the Superstar II GPS receiver

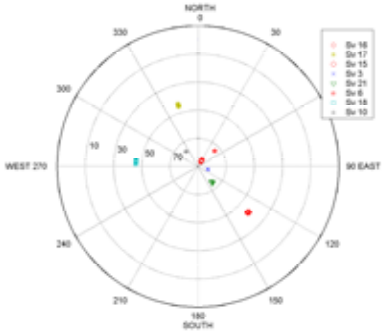


Figure 6.4: Skyplot for the Superstar II GPS receiver.

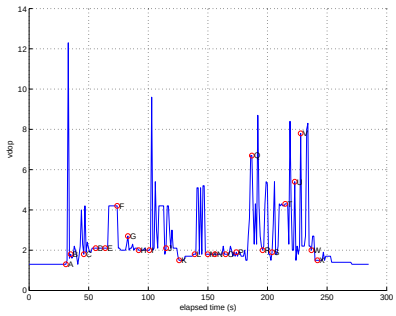


Figure 6.5: VDOP for the Superstar II GPS receiver during the entire run

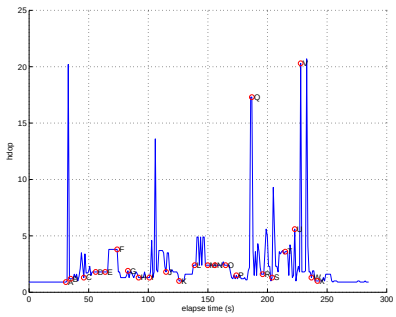


Figure 6.6: HDOP for the Superstar II GPS receiver during the entire run

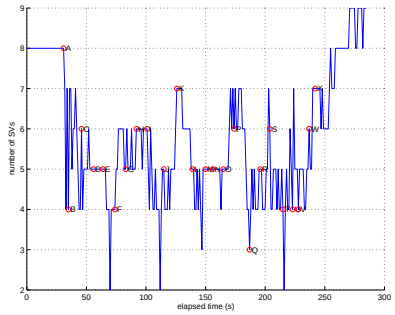


Figure 6.7: Number of satellites used by the Superstar II GPS receiver to calculate the position during the entire run

# 7 Navigation Filter

This chapter is divided into two sections describing the implementation and result for a loosely coupled filter and a tightly coupled filter respectively.

## 7.1 Loosely-Coupled Extended Kalman Filter

### 7.1.1 Implementation

The loosely coupled extended Kalman filter uses inertial navigation system (INS) sensors to predict the position, velocity and attitude. By using 3 gyros and 3 accelerometers mounted in the inertial measurement unit (IMU) the navigation states position, velocity and attitude is determined by propagating the non-linear navigation equations (2.17) forward in time. The filter implementation is visualised in figure 7.1. The INS predict the position, velocity and attitude. When a GPS position is available the Kalman filter uses the difference between the measured GPS-position and the predicted INS-position. The INS predicted navigation states are corrected by the Kalman filter navigation error states.

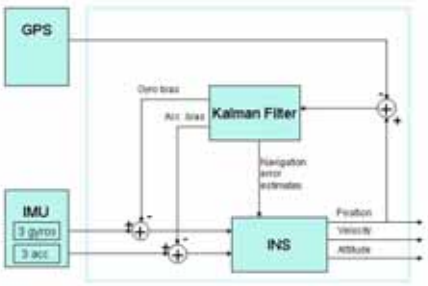


Figure 7.1: Block diagram of the loosely coupled EKF.

#### 7.1.1.1 System Model

The total error state vector of the loosely-coupled extended Kalman filter is

$$\epsilon = \begin{bmatrix} \epsilon_1 \\ \epsilon_2 \end{bmatrix} = \begin{bmatrix} \boldsymbol{\Psi} \\ \delta\mathbf{v} \\ \delta\mathbf{x} \\ \mathbf{d} \\ \mathbf{b} \end{bmatrix} \tag{7.1}$$

Where $\varepsilon_1 = \begin{bmatrix} \mathbf{\Psi} \\ \delta\mathbf{v} \\ \delta\mathbf{x} \end{bmatrix}$ represents the nine navigation errors, attitude, velocity and positional errors respectively. $\varepsilon_2 = \begin{bmatrix} \mathbf{d} \\ \mathbf{b} \end{bmatrix}$ are the sensor errors, here gyro- and accelerometer bias respectively. The linearised system can be written as

$$\frac{d}{dt}\epsilon(t) = F(t)\,\epsilon(t) + G(t)\,\mathbf{w}(t) \tag{7.2}$$

where

$$F = \begin{bmatrix} F_1(t) & F_2(t) \\ 0_{6\times 9} & 0_{6\times 6} \end{bmatrix} \tag{7.3}$$

Where $F_1$ is the error dynamics matrix of the navigation equations (2.17). $F_2$ transforms the IMU errors from body coordinates to ECEF-coordinates.

$$F_1 = \begin{bmatrix} -\Omega_{ie}^e & 0_{3\times 3} & 0_{3\times 3} \\ \mathbf{a}\times & -2\Omega_{ie}^e & \bigtriangledown \\ 0_{3\times 3} & I_{3\times 3} & 0_{3\times 3} \end{bmatrix} \tag{7.4}$$

$$F_2 = \begin{bmatrix} -C_b^e & 0_{3\times 3} \\ 0_{3\times 3} & C_b^e \\ 0_{3\times 3} & 0_{3\times 3} \end{bmatrix} \tag{7.5}$$

$\Omega_{ie}^e$ is the skew-symmetric matrix described in (2.13). $I_{3\times 3}$ is a identity matrix of size $3\times 3$ and $C_b^e$ is the directional cosine matrix that transforms coordinates from the body frame (b-frame) to the ECEF-frame (e-frame). $\bigtriangledown$ is a matrix which contains the tensor of gravitational gradients $\Gamma$ and centripetal acceleration due to the earth rotation. It can be expressed as $\bigtriangledown = -(\Omega\Omega - \Gamma)$. The gravitational model used in the implementation of the filters is a model of a spherical earth described in [13].
The $G(t)$ matrix in (7.2) describes how the noise $\mathbf{w}(t)$ effects the system, where $\mathbf{w}(t)$ is a white Gaussian process. In the implementation of the loosely coupled filter the system noise $\mathbf{w}(t)$ is assumed to be additive noise in the IMU sensors, accelerometers and gyros.

$$\mathbf{w}(t) = \begin{bmatrix} \mathbf{w}_{gyro}(t) \\ \mathbf{w}_{acc}(t) \end{bmatrix} \tag{7.6}$$

In the IMU calibration test in section 5.2.3 it was concluded that the IMU output also contains other error processes. These error sources could also be modelled to get a more accurate model of the IMU. The white noise from the gyros only effects the attitude states $\Psi$, and the accelerometer white noise effects the velocity states $\mathbf{v}$. the $G(t)$ matrix therefore contains two direction cosine matrices.

$$G = \begin{bmatrix} -C_b^e & 0_{3\times 3} \\ 0_{3\times 3} & C_b^e \\ 0_{9\times 3} & 0_{9\times 3} \end{bmatrix} \tag{7.7}$$

### Discrete system

The system (7.2) is a continuous linear system. In order to implement the system it has to be rewritten into discrete form. In order to calculate the error covariance, $P_k$, the transition matrix , $\Phi_k$, of the linearised system in (7.2) is needed. $\Phi$ may be expressed as

$$\Phi(t_k, t_{k-1}) \approx I + F\Delta t \tag{7.8}$$

valid only for small values of $\Delta t = t_k - t_{k-1}$. For more information see [17] and [13]. The noise must be discrete as well. The discrete system noise covariance $\Theta_k$ depends on the matrix $G_k$ which is time dependent. The system noise covariance will be discretized as

$$\Theta_k = G_k Q \Delta t G_k^T \tag{7.9}$$

Where $Q$ is a diagonal matrix containing spectral densities of the gyro and accelerometer noise.

#### 7.1.1.2 Observation Model

The observations come from the GPS in the form of a position estimate. The observation model can be written as

$$\mathbf{y} = \mathbf{h}(\mathbf{x}) + \mathbf{v} \tag{7.10}$$

Where $\mathbf{h}(\mathbf{x})$ simply is the GPS position estimate, as

$$\mathbf{h}(\mathbf{x}) = \begin{bmatrix} x \\ y \\ z \end{bmatrix} \tag{7.11}$$

Here $\mathbf{x} = (x, y, z)^T$ is the user position.
The linearized observation model can then be expressed as

$$H = \begin{bmatrix} 0_{1\times3} & 0_{1\times3} & 1 & 0 & 0 & 0_{1\times3} & 0_{1\times3} \\ 0_{1\times3} & 0_{1\times3} & 0 & 1 & 0 & 0_{1\times3} & 0_{1\times3} \\ 0_{1\times3} & 0_{1\times3} & 0 & 0 & 1 & 0_{1\times3} & 0_{1\times3} \end{bmatrix} \tag{7.12}$$

#### 7.1.1.3 Filter Structure

The extended Kalman filter algorithms are not given here in details but can be found in [13]. Instead an overview of the calculations of the loosely coupled filter is given in the form of a flow chart in Figure 7.2.

First the filter is initialized by setting the initial Kalman state vector and the corresponding covariance matrix. The filter then enters a loop as long as IMU data exists. The loop begins by getting the current system matrix with associated accelerometer data (used in $F_1$, see (7.4)) where bias has been compensated for. Then the discrete state transition matrix $\Phi$ and covariance matrix $\Theta$ is calculated according to (7.8) and (7.9) respectively. In the next step the prediction is calculated. This means that a state estimate for time $k+1$ given measurements to time $k$ and its corresponding covariance is computed according to [17]. The described prediction step is repeated until a new measurement is available. Then the measurement update is performed by getting the new observation and then calculating the Kalman gain and the innovation.

Taking the product between the Kalman gain and the innovation gives a correction term to be added to the previous estimate. Before the filter state vector is measurement updated, a diverge test is performed in the first three elements of the state vector, the angular errors.

#### 7.1.1.4 Filter Parameters

To be able to compare the loosely coupled and the tightly coupled filter the filter settings should be set to the same values except for the measurement noise covariance, $R$. For the loosely coupled Kalman filter the measurement noise covariance was initially determined by collecting GPS position fixes from

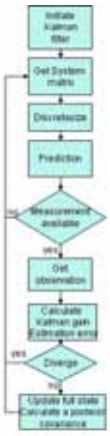

Figure 7.2: Flow chart for the computations of the loosely coupled Kalman filter

the Superstar II GPS receiver. This data was used to calculate the standard deviation. After using these standard deviations in the measurement noise covariance matrix the values was slightly decreased to get a better filter performance. The final measurement noise parameters after the filter tuning are presented in Table 7.1.The initial state vector covariance are presented in Table 7.2 and the system noise in Table 7.3.

Table 7.1: Square root of the diagonal elements of the measurement noise covariance matrix $R$

| | $x$ | $y$ | $z$ |
|---|---|---|---|
| $[m]$ | 1.8 | 1.4 | 2 |

Table 7.2: Square roots of the diagonal elements in the initial error covariance matrix $P_0$. All values are presented in three dimensions.

| Attitude $[^\circ]$ | Velocity $[m/s]$ | Position $[m]$ | Gyro Bias $[rad/s]$ | Acc Bias $[m/s^2]$ |
|---|---|---|---|---|
| 5 (roll) | 1 | 10 | $5\mu$ | $5m$ |
| 5 (pitch) | 1 | 10 | $5\mu$ | $5m$ |
| 7 (yaw) | 1 | 10 | $5\mu$ | $5m$ |

Table 7.3: square root of the diagonal elements in the initial Kalman filter system noise matrix $Q$. The noise variance for the attitude and velocity reflect the gyro and accelerometer white noise spectral densities, respectively.

| Attitude $[rad/\sqrt{s}]$ | Velocity $\left[m/s^2/\sqrt{Hz}\right]$ |
|---|---|
| $1.1167 \cdot 10^{-3}$ | $7.888 \cdot 10^{-3} \cdot 20$ |
| $1.1023 \cdot 10^{-3}$ | $6.7713 \cdot 10^{-3} \cdot 20$ |
| $9.945 \cdot 10^{-4}$ | $9.3595 \cdot 10^{-3} \cdot 20$ |

### 7.1.2 Experimental Results

#### 7.1.2.1 Estimated Position

These results are based on the data from lap-nr 5 of the five laps conducted around the Ursvik test track. These data were chosen because of the number of available satellites.

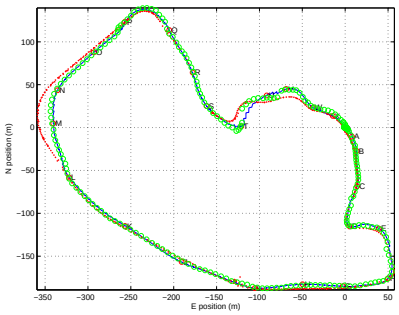


Figure 7.3: GPS measurements. The reference GPS (red dots) are compared to the Superstar II GPS (green circles) and the loosely coupled filter estimate (blue line) of the vehicle trajectory. Note that due to the vibration sensitive reference GPS (with long outages), measurements from five laps are here overlaid. The error of the reference GPS is about $4$ cm $(SEP)$.The labels A to X is described in Table 6.1 to help to keep track of the vehicles position at a certain time.

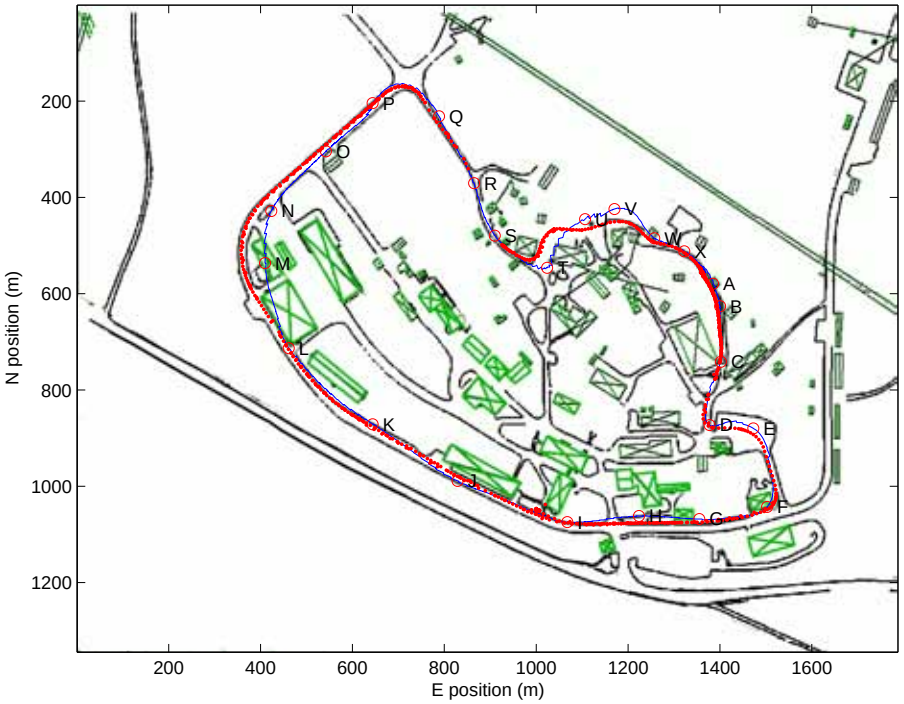


Figure 7.4: Ursvik road map with buildings. The loosely-coupled filter estimate (blue line) of the vehicle trajectory together with the reference GPS measurements (red dots).Note that due to the vibration sensitive reference GPS (with long outages), measurements from five laps are here overlaid. The error of the reference GPS is about $4$ cm $(SEP)$.

During the tests the reference GPS in section 4.2 has been used. It is very sensitive to vibrations and accelerations which give rise to relatively long

GPS-outages. To be able to compare and analyze the filter estimates of the vehicle trajectory reference GPS measurements from multiple laps has been overlaid in Figure 7.3 and 7.4. However when there is a reference GPS position-fix its positional error is in the order of 4 cm ($SEP$). Figure 7.3 shows the comparison between the filter generated position, the Superstar II position and the reference position. To be able to analyze filter performance, the resulting filter estimate of the vehicle trajectory has been plotted on a Ursvik road map containing information about surrounding buildings (marked green), see Figure 7.4 which also has the reference GPS trajectory. In Figure 7.5 the innovations in e-frame for $x, y$ and $z$ axes with associated $3\sigma$ limit can be seen. It is of particular interest to analyze the time intervals when the innovation exceeds the corresponding $3\sigma$ intervals. This is an indication that the filter has been exposed for an out-lier meaning that it was not designed for this event. All time intervals when this happens are listed in and described in Table 7.4 It should also be noted that in the case of the loosely coupled navigation filter the innovation is in fact three element measurement residual in position expressed in the $e$-frame (ECEF). Later in this chapter, for the tightly coupled filter, the innovation consists of measurement residual in pseudo distance for all visible satellites. The estimation error in position in a ENU local frame are

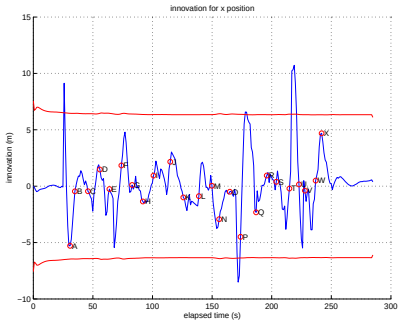


(a) x innovation in meters

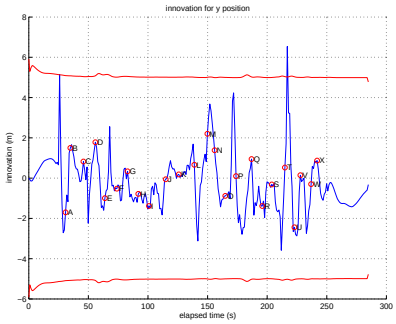


(b) y innovation in meters

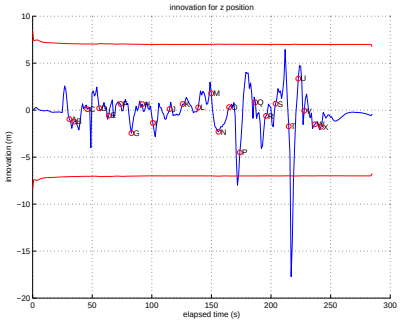


(c) z innovation in meters

Figure 7.5: Innovations of the loosely-coupled navigation filter for the entire run. In $e$-frame.

plotted together with the corresponding $3\sigma$ intervals. The navigation equations being used when designing the Kalman filter has been expressed in the $e$-frame (ECEF). The reason for evaluating the estimation errors in a local ENU-

frame and not the $e$-frame is easier to grasp the error magnitude when looking at the trajectory in Figure 7.4. Note that the estimation error is calculated as the difference between the filter position and the reference GPS position. Therefore the estimation errors can only be evaluated when there is a reference GPS measurement available. Due to the sensitive reference GPS receiver there are relatively long time-intervals without estimation errors. The Superstar II measurements are used as filter observations and the difference between the Superstar II measurements and the reference position is also plotted, with green circles, in Figure 7.6 There are two interesting time-intervals of the estimated

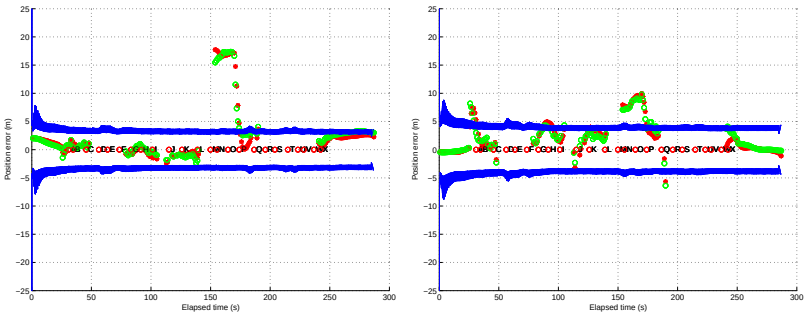


(a) Position estimation error in east (E)axis

(b) Position estimation error in north (N) axis

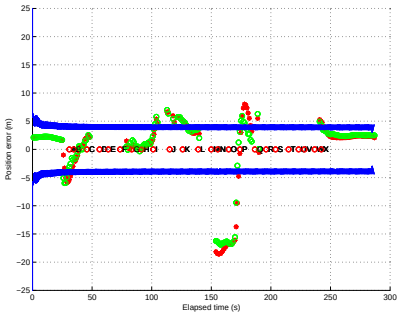


(c) Position estimation error in up (U) axis

Figure 7.6: Estimation error in position in a ENU local frame. The estimation errors in position are marked with red stars. The Superstar II measurements are used as filter observation and re marked with green circles. Note that the estimation error is calculated as the difference between filter position and reference GPS position: lack of GPS reference data is the reason for the gaps in estimation error where it can not be evaluated.

trajectory that will be investigated. It is in particular the effect of (1) poor geometrical satellite constellation and (2) frequent switching of satellites that will be discussed here. It can be seen in Figure 7.4 and 7.6 that during the time interval labels $L - O$ the filter position differs from the reference system with approximately $20\,m$ in the E axis, $10\,m$ in the N axis and $22\,m$ in the U axis. However the innovations in Figure 7.5 does not exceed the $3\sigma$ intervals during this time interval. In Figure 7.3 and 7.6 it is clear that the position from the Superstar II receiver also differs from the reference position. The buildings on the north-east side of the vehicle obstructs the satellites. Figure

Table 7.4: Summary of time-intervals when innovation exceed the $3\sigma$ intervals.

| Position | Time [s] | Description/Reason |
|---|---|---|
| Start-$A$ | $0-31$ | Vehicle starts moving and the velocity changes rapidly from zero. |
| $O-P$ | $165-174$ | Loss of satellite changing the satellite constellation |
| $P-Q$ | $174-186$ | Loss of satellites due to forest above and on both sides of the road. |
| $T-U$ | $215-223$ | Gain of a satellite. |

6.7 shows that the position estimate from the Superstar II receiver is only based on four satellites and for a short period of time the number drops to three between $L$ and $M$. The sky-view in Figure 6.4 and the availability plot in Figure 6.3 shows all these satellites (3-5 satellites, Sv nr.: 21, 18, 16, 15, 3) lies in north-west to south-east bound direction, indicating that the position estimate has a larger position error lateral to the direction of motion. It can also be seen in Figure 6.6 and Table 6.1 that the HDOP during the time interval $L-O$ is oscillating between 2.5 and 5, indicating a poor geometrical satellite constellation. The Superstar II GPS errors naturally influences the performance of the loosely-coupled navigation filter. It is also important to note that the information about poor geometrical constellation is not used in this filter. Only the position-fix calculated by the Superstar II GPS receiver is used as an observation. However is should be noted in Figure 7.3 that the navigation filter uses IMU-information. In the rather sharp turn the estimated trajectory has even larger lateral errors than of the Superstar II GPS receiver. This is due to that the INS senses the turning motion.

During the time-interval labels $T-W$ it can be seen in Figure 7.3 that the INS and GPS are in conflict with each other, due to the jagged-shaped filter trajectory revealing that the GPS heading information and the INS heading information is wide part. This is due to many loss-of-tracking and reacquiring of satellites during this time interval. This can clearly be seen in Figure 6.7 showing a sever flickering in the number of satellites. The effect of this abrupt changes in Superstar II position and thereby also in the loosely-coupled position estimate. The filter can not handle these geometrical changes as can be seen in Figure 7.3.

#### 7.1.2.2 Attitude Errors

Figure 7.7 shows the orientation of the vehicle during the entire run, plotted with the associated $3\sigma$ intervals. The attitude standard deviation for all three error states, Figure 7.8, shows that the pitch and roll estimates converge faster than the yaw estimate. This is due to the fact that the pitch and roll estimation can take advantage of that the accelerometers senses the gravitation whenever there is an attitude error present. When the Kalman filter parameters are tuned it is important to take advantage and use knowledge of the conditions during the test. For example the yaw (direction/heading) estimate uses information from the yaw gyro (angular changes in heading), the accelerometers (direction changes of the velocity vector) and the GPS (velocity vector estimate). However during periods when the vehicle is driving slow or standing still the GPS and the accelerometers contains very little information about the heading and therefore it is mainly the gyro readings that do contribute to improve the heading estimate. The attitude estimation error of the filter has been calculated as the difference between the navigation filter attitude angle estimates and the reference GPS attitude estimates. However, since the ref-

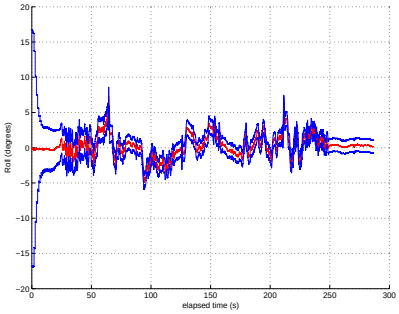


(a) Estimated roll angle.

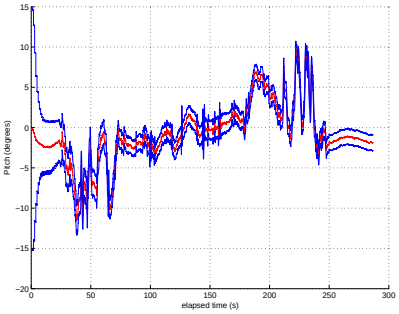


(b) Estimated pitch angle.

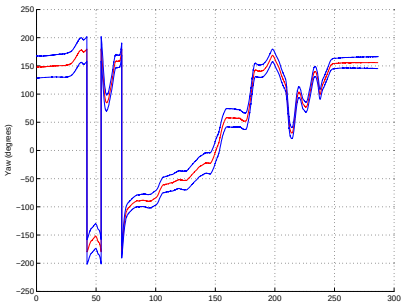


(c) Estimated yaw angle.

Figure 7.7: The estimated attitude angles expressed in the local frame with the corresponding $3\sigma$ intervals.

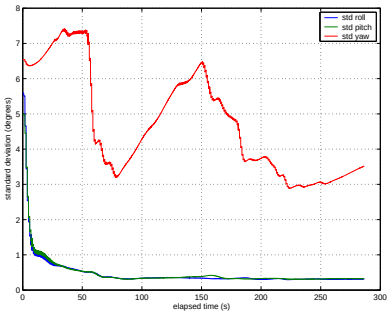


Figure 7.8: Standard deviation of the estimated attitude angles.

erence GPS system only is based on two antennas the estimation errors could only be evaluated in pitch- and heading-angle. Also due to the very vibration sensitive reference GPS there are rather long time intervals where the estimation error unfortunately could not be evaluated due to missing reference data, Figure 7.9. It should be noted that when the vehicle is stationary at the end of the experimental run (reference measurements can be trusted) the pitch- and yaw-errors are in the order of 0.5° and 5° respectively. there is a slow error growth in yaw error from 250 seconds when the car is standing still. The reason is that the Superstar II GPS do not contribute with heading information when it is stationary resulting in that the navigation filter has to rely on the inertial

sensors with its increasing error.

Since angular errors give rise to large positional errors it is vital to be able to analyze these estimation errors. Therefore, in the future experiments a more robust reference system is needed.

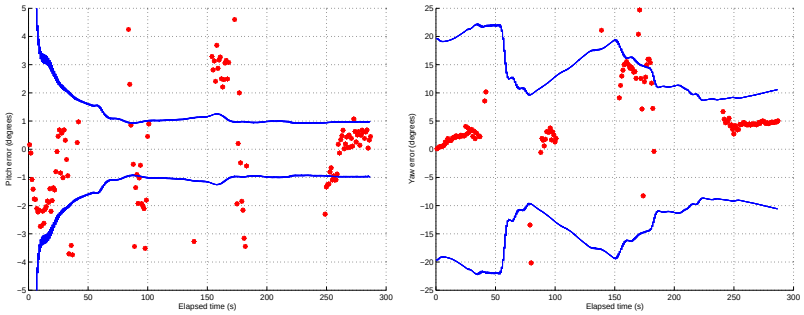


(a) Pitch error. (b) Yaw error.

Figure 7.9: Estimation error in pitch and yaw with corresponding $3\sigma$ intervals.

#### 7.1.2.3 Gyro Bias

The initial value of the gyro bias and its covariance has been chosen according to Table 5.5 and 7.2, and is based on the calibration result presented in chapter 5. In Figure 7.10 and 7.11 it can clearly be seen that the roll- and pitch-gyro bias estimates converge faster than the yaw-gyro bias estimate. This is most likely due to the low excitation in the heading channel which is needed for convergence.

To improve this a special initial motion is required which for example could consist of a slalom like trajectory.

It is quite difficult to really make any certain performance conclusions for the gyro bias estimation. The bias determined in the calibration was done in a laboratory environment with room temperature and the experiments was conducted outside. Most likely the IMU-biases are changing with the temperature even though the manufacturer has temperature compensated the sensor unit.

During future experiments it is therefore important to stabilize the ambient temperature and to monitor and store possible deviations.

There are no changes in sign of the estimates and the estimates does not change radically from the initial guess originating from the calibration which indicates that the estimator is working properly.

#### 7.1.2.4 Accelerometer Bias

The initial value of the accelerometer bias and its corresponding covariance has been chosen according to Table 5.1 and 7.2, and is based on the calibration result presented in chapter 5. In Figure 7.12 and 7.13 it clearly can be seen that the $x$- and $y$-accelerometer bias estimates converge slower than the $z$-accelerometer bias. This is most likely due to that the gravity component effects the $z$ channel at all times and therefore the estimation can converge faster.

Since the bias estimates changes so much during a experimental run, particularly in the $y$-accelerometer bias estimate, it indicates that the filter might

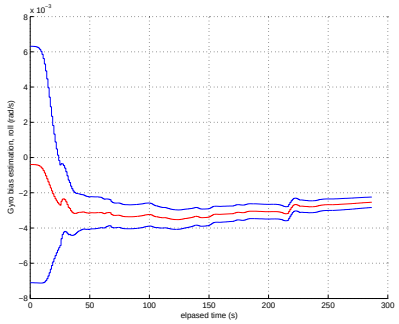


(a) Gyro bias for roll-gyro ($x$).

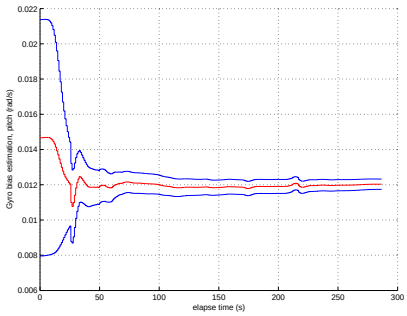


(b) Gyro bias for pitch-gyro ($y$).

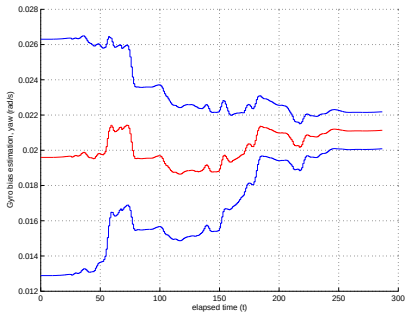


(c) Gyro bias for yaw-gyro ($z$).

Figure 7.10: Estimated gyro bias with corresponding $3\sigma$ intervals (rad/s).

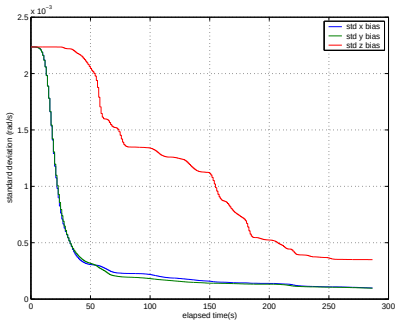


Figure 7.11: Standard deviation of the estimated gyro bias (rad/s).

be exposed to un-modelled errors. The temperature changes can be one reason. Also the model of the gravity need to be improved.

During future experiments it is important to stabilize the ambient temperature and to monitor and store possible deviations.

#### 7.1.2.5 Summary of Results for The Loosely Coupled Filter

For the major part of the test course the position error lies within the $3\sigma$ intervals. But the position estimate has problems when a satellite tracking is lost or a satellite is reacquired. The attitude estimates are good. The gyro and

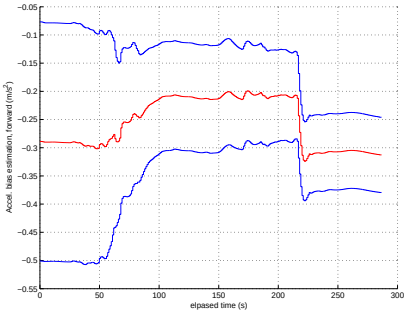


(a) Accelerometer bias estimate forward($x$).

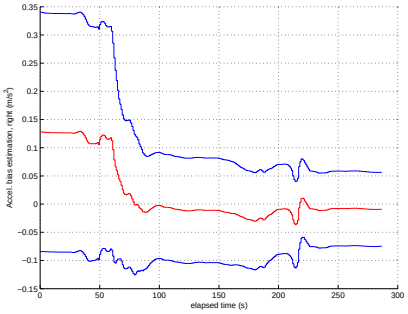


(b) Accelerometer bias estimate side($y$).

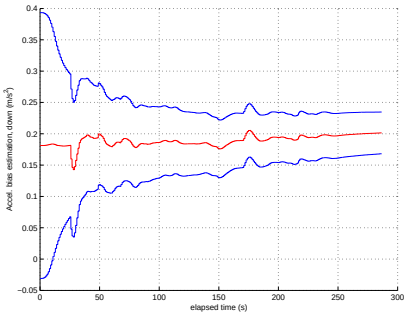


(c) Accelerometer bias estimate up($z$).

Figure 7.12: Estimated accelerometer bias in m/s$^2$

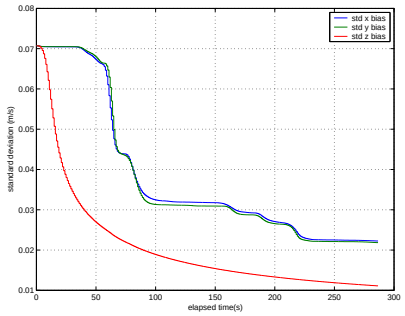


Figure 7.13: Standard deviation of the accelerometer bias in m/s

accelerometer biases converge. The results can be improved by expanding the error model for the accelerometers and gyros and maybe make the measurement covariance time dependent so that it depends upon the number of satellites and the constellation.

## 7.2 Tightly-Coupled Extended Kalman Filter

### 7.2.1 Implementation

The tightly coupled extended Kalman filter uses an INS to predict the position, velocity and attitude. The observations consists of GPS pseudoranges. The filter implementation is visualized in Figure 7.14.

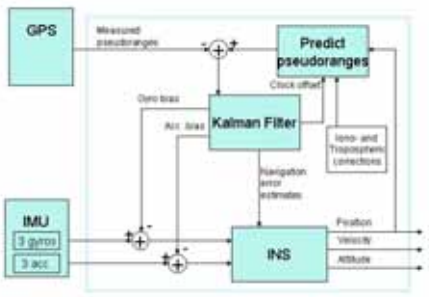


Figure 7.14: The INS sensors are used to predict the position, velocity and attitude by using the navigation equations in the INS-block. Which is then used to predict the pseudoranges to all visible satellites. The Kalman filter then uses the difference in pseudoranges (INS-predicted minus GPS-measured) as an observation.

#### 7.2.1.1 System Model

The total error state vector of the tightly-coupled extended Kalman filter is

$$\epsilon = \begin{bmatrix} \epsilon_1 \\ \epsilon_2 \\ \epsilon_3 \end{bmatrix} = \begin{bmatrix} \boldsymbol{\Psi} \\ \delta\mathbf{v} \\ \delta\mathbf{x} \\ \mathbf{d} \\ \mathbf{b} \\ \delta\left(c\delta t\right) \end{bmatrix} \tag{7.13}$$

Where $\varepsilon_1 = \begin{bmatrix} \boldsymbol{\Psi} \\ \delta\mathbf{v} \\ \delta\mathbf{x} \end{bmatrix}$ represents the navigation errors, attitude, velocity and positional errors respectively. $\varepsilon_2 = \begin{bmatrix} \mathbf{d} \\ \mathbf{b} \end{bmatrix}$ are the sensor errors, here gyro- and accelerometer bias respectively. $\varepsilon_3 = \delta\left(c\delta t\right)$ is the error state of the receiver clock error. The linearised system can be written as

$$\frac{d}{dt}\epsilon\left(t\right) = F\left(t\right)\epsilon\left(t\right) + G\left(t\right)\mathbf{w}\left(t\right) \tag{7.14}$$

where

$$F = \begin{bmatrix} F_1\left(t\right) & F_2\left(t\right) & 0_{9\times1} \\ 0_{6\times9} & 0_{6\times6} & 0_{6\times1} \\ 0_{1\times9} & 0_{1\times9} & 0_{1\times1} \end{bmatrix} \tag{7.15}$$

$F_1$ is the error dynamic matrix (7.4) and $F_2$ transforms the IMU sensor readings from body to earth frame according to (7.5).

The $G(t)$ matrix in (7.14) describes how the sensor noise effects the system. The only difference from the loosely coupled filter is the additional receiver clock error state which result in

$$G = \begin{bmatrix} -C_b^e & 0_{3\times 3} \\ 0_{3\times 3} & C_b^e \\ 0_{10\times 3} & 0_{10\times 3} \end{bmatrix}$$

The discrete system is calculated in the same manner as in the loosely coupled filter, see subsection 7.1.1.

#### 7.2.1.2 Observation Model

The observation model for the tightly coupled Kalman filter is based upon the pseudoranges from the GPS receiver. The GPS measures the pseudorange for every visible satellite. The observations are modelled as the true geometrical distance from the user to the satellite, together with a receiver clock bias, satellite clock error, ionospheric , tropospheric delay and white noise. The observation model can be written as

$$\mathbf{y} = \mathbf{h}\left(\mathbf{x}, c\delta t\right) + \mathbf{v} \tag{7.16}$$

where

$$\mathbf{h}\left(\mathbf{x}, c\delta t\right) = \begin{pmatrix} \sqrt{\left(x - x^1\right)^2 + \left(y - y^1\right)^2 + \left(z - z^1\right)^2} + c\delta t - \delta t_{sv}^1 + T_{Iono}^1 + T_{Tropo}^1 \\ \sqrt{\left(x - x^2\right)^2 + \left(y - y^2\right)^2 + \left(z - z^2\right)^2} + c\delta t - \delta t_{sv}^2 + T_{Iono}^2 + T_{Tropo}^2 \\ \vdots \\ \sqrt{\left(x - x^p\right)^2 + \left(y - y^p\right)^2 + \left(z - z^p\right)^2} + c\delta t - \delta t_{sv}^p + T_{Iono}^p + T_{Tropo}^p \end{pmatrix} \tag{7.17}$$

Here $\mathbf{x} = (x, y, z)^T$ is the user position, $(x^n, y^n, z^n)$ is the position of the $n$:th satellite. $c\delta t$ is the user clock bias. $\delta t_{sv}^n$, $T_{Iono}^n$ and $T_{Tropo}^n$ is the satellite clock error, ionospheric and tropospheric delay for the $n$:th satellite respectively.
The linearized observation matrix, $H$, is given by taking the partial derivatives of the non-linear observation equation $h$.

$$H = \begin{bmatrix} 0_{1\times 3} & 0_{1\times 3} & \mathbf{e}_{1\times 3}^1 & 0_{1\times 3} & 0_{1\times 3} & 1 \\ 0_{1\times 3} & 0_{1\times 3} & \mathbf{e}_{1\times 3}^2 & 0_{1\times 3} & 0_{1\times 3} & 1 \\ \vdots & \vdots & \vdots & \vdots & \vdots & \vdots \\ 0_{1\times 3} & 0_{1\times 3} & \mathbf{e}_{1\times 3}^p & 0_{1\times 3} & 0_{1\times 3} & 1 \end{bmatrix} \tag{7.18}$$

$$\mathbf{e}_{1\times 3}^n = \left[ \left( \frac{\hat{x} - x^n}{\hat{r}^n} \right) \left( \frac{\hat{y} - y^n}{\hat{r}^n} \right) \left( \frac{\hat{z} - z^n}{\hat{r}^n} \right) \right] \tag{7.19}$$

where $\hat{r}^n$ is an estimate of the distance between the estimated position, $(\hat{x}, \hat{y}, \hat{z})$, to the $n$:th satellite position $(x^n, y^n, z^n)^T$ , where $n = 1, ..., p$:

$$\hat{r}^n = \sqrt{\left(\hat{x} - x^n\right)^2 + \left(\hat{y} - y^n\right)^2 + \left(\hat{z} - z^n\right)^2} \tag{7.20}$$

#### 7.2.1.3 Filter Structure

Since the extended Kalman filter is a recursive algorithm, the filter needs to be initialised with the initial Kalman state vector and the corresponding covariance matrix. The filter then loops as long as there are IMU sensor readings. The filter starts by getting the system matrix with the current bias corrected accelerometer readings. The discrete state transition matrix $\Phi$ and covariance

matrix $\Theta$ is calculated. A prediction is made with the current IMU readings. If GPS measurements exist for the current time, then the filter fetches the observation model. The observation model consists of two steps. The first step is to calculate the GPS message time of transmission ,$t_{sv}$ ,to be able to estimate the satellite positions and then estimate the satellite clock error and the ionospheric and tropospheric delay. The ionospheric delay is estimated using the Clobuchar model see [1]. The tropospheric delay is estimated using a standard model with standard atmospheric parameters. The satellite positions are then updated. In the second step the observation model described in section 7.2.1.2 is evaluated for the time of interest. When the observation is evaluated the Kalman gain and the innovation is calculated and multiplied with each other resulting in a correction term. If not the full state and covariance is updated. Figure 7.15 shows a overview of the filter structure.

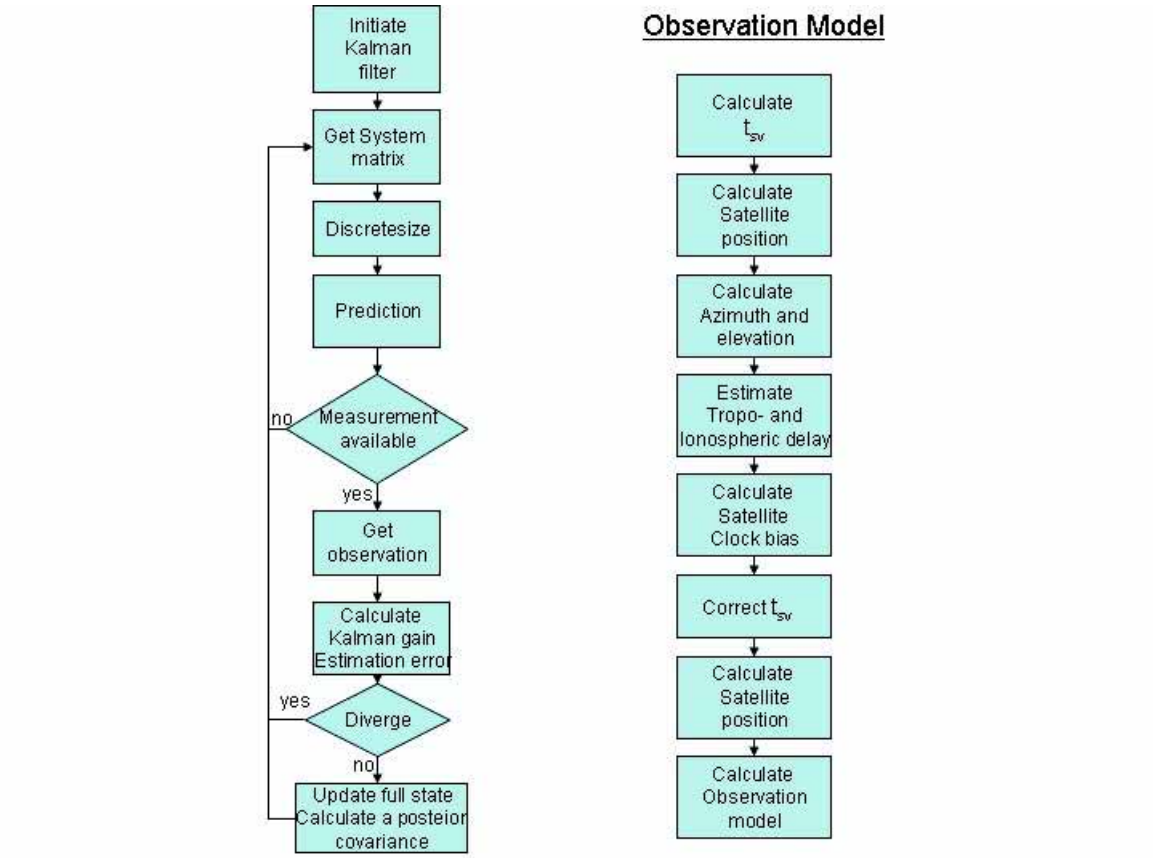


Figure 7.15: Filter structure for tightly coupled Kalman filter

#### 7.2.1.4 Filter Parameters

To be able to compare the loosely coupled filter results with the tightly coupled filter, the filter parameters is the same for both filters besides the measurement noise covariance. The initial full state is set to predefined values, the start position taken from the reference GPS the initial attitude is also taken from the reference GPS, the velocity is known to be zero since we are stationary at the beginning, the gyro and accelerometer biases is taken from the calibration. The only unknown value is the user clock bias, which is set to zero, since we do not expect it to be any user clock bias since the Superstar GPS clock is steered,

meaning that the user clock is compensated for clock biases. The initial values of the covariance matrix, $P_0$, are presented in Table 7.5. The measurement covariance ,$R$, reflect the error such as errors in the ionospheric and tropospheric models, multipath, satellite and receiver clock offset and other uncorrelated noise. The measurements is assumed to be uncorrelated, with variance $\sigma^2 = (4\,[m])^2$. Another tunable parameter is the system noise covariance, $Q$.

Table 7.5: Square roots of the diagonal elements in the initial error covariance matrix $P_0$. All values except the user clock bias are presented in three dimensions.

| Attitude $[^\circ]$ | Velocity $[m/s]$ | Position $[m]$ | Gyro Bias $[rad/s]$ | Acc Bias $\left[m/s^2\right]$ | User Clock Bias $[m]$ |
|---|---|---|---|---|---|
| 5 (roll) | 1 | 10 | $5\mu$ | $5m$ | 10 |
| 5 (pitch) | 1 | 10 | $5\mu$ | $5m$ | |
| 7 (yaw) | 1 | 10 | $5\mu$ | $5m$ | |

The $R$ matrix has been fixed then the $Q$ matrix has been tuned until the filter performance is satisfactory. $Q$ started out with the power spectral density for the gyros and accelerometers from the calibration, but to decrease the position and attitude error the accelerometer noise had to be multiplied by a factor 20. The increased accelerometer noise can be due to unmodelled errors, scale factor and misalignment. The final system noise covariance is presented in Table 7.6.

Table 7.6: square root of the diagonal elements in the initial Kalman filter system noise matrix $Q$. The noise variance for the attitude and velocity reflect the gyro and accelerometer white noise spectral densities, respectively.

| Attitude $[rad/\sqrt{s}]$ | Velocity $\left[m/s^2/\sqrt{Hz}\right]$ |
|---|---|
| $1.1 \cdot 10^{-3}$ | $7.9 \cdot 10^{-3} \cdot 20$ |
| $1.1 \cdot 10^{-3}$ | $6.8 \cdot 10^{-3} \cdot 20$ |
| $1 \cdot 10^{-4}$ | $9.4 \cdot 10^{-3} \cdot 20$ |

### 7.2.2 Experimental Result

As mentioned the Superstar II GPS receiver can produce pseudoranges with a $10\,Hz$ frequency. To be able to compare the results from the loosely coupled filter with the tightly coupled, the observations is set to $1\,Hz$ as the observation update in the loosely coupled filter.

#### 7.2.2.1 Estimated Position

These results are based on the data from lap-nr 5 of the five laps conducted around the Ursvik test track. These data was chosen because of the number of available satellites.

During the tests the reference GPS in section 4.2 has been used. It is very sensitive to vibrations and accelerations which give rise to relatively long GPS-outages. To be able to compare and analyze the filter estimates of the vehicle trajectory reference GPS measurements from multiple laps has been overlaid in Figure 7.16. However when there is a reference GPS position-fix its positional error is in the order of 4 cm ($SEP$). To be able to analyze filter performance, the resulting filter estimate of the vehicle trajectory has been plotted on a Ursvik road map containing information about surrounding buildings (marked green), see Figure 7.4 which also has the reference GPS trajectory.

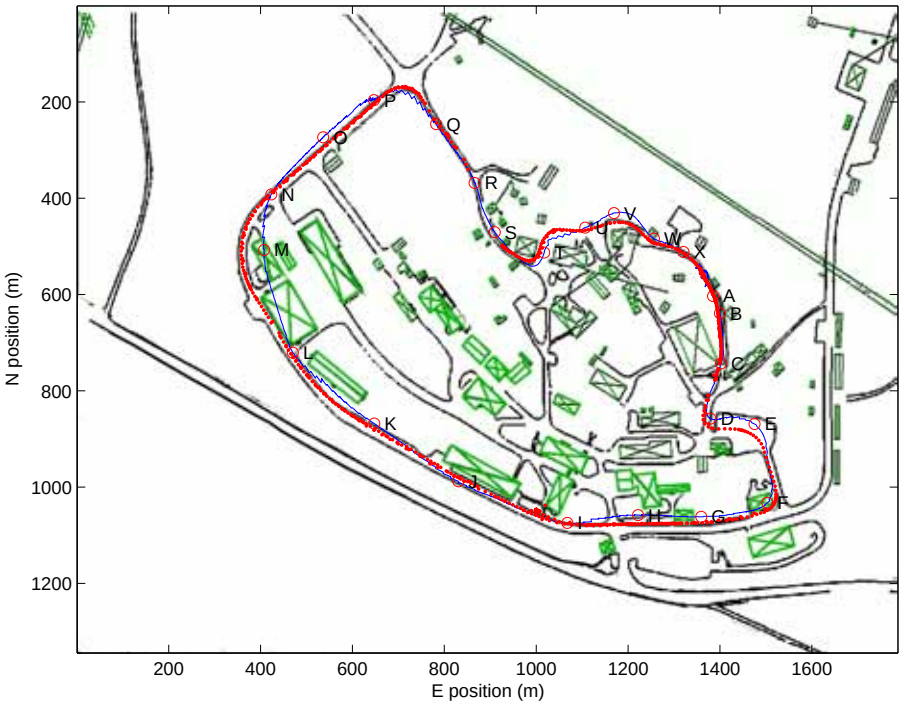


Figure 7.16: Ursvik road map with buildings. The tightly-coupled filter estimate (blue line) of the vehicle trajectory together with the reference GPS measurements (red dots).Note that due to the vibration sensitive reference GPS (with long outages), measurements from five laps are here overlaid. The error of the reference GPS is about 4 cm ($SEP$). The labels A to X is described in Table 6.1 to help to keep track of the vehicles position at a certain time.

In Figure 7.17 the innovations in $e$-frame with associated $3\sigma$ intervals can be seen. The innovation consist measurement residual in pseudo distance for all visible satellites. The innovations only exceeds the $3\sigma$ intervals ones, just before the $P$ time label. this is due to reacquiring of a satellite. It can clearly be seen that the estimated standard deviation of the tightly-coupled filter position, Figure 7.18, is highly correlated with the loss-of-tracking and reacquiring of satellites, this can be seen by comparing the standard deviation with the times of loss-of-tracking and reacquiring of satellites in Figure 6.3.

The estimation error in position in a ENU local frame are plotted together with the corresponding $3\sigma$ intervals, Figure 7.19. The navigation equations being used when designing the Kalman filter has been expressed in the $e$-frame (ECEF). Note that the estimation error is calculated as the difference between the filter position and the reference GPS position. Therefore the estimation errors can only be evaluated when there is a reference GPS measurement available. Due to the sensitive reference GPS receiver there are relatively long time-intervals without estimation errors. In the loosely coupled filter in 7.1.2.1 two sections of the estimated trajectory were investigated, section $L - O$ and section $T - W$ of the test course. It is in particular the effect of (1) poor geometrical satellite constellation and (2) frequent switching of satellites that will be discussed here. It can be seen in Figure 7.16 and 7.19 that during the time interval labels $L - O$ the filter position differs from the reference system with approximately 18 $m$ in the E axis, 22 $m$ in the N axis and 15 $m$ in the U axis. Just as discussed in the loosely coupled filter, the available satellites drops. The sky-view in Figure 6.4 and the availability plot in Figure 6.3 shows

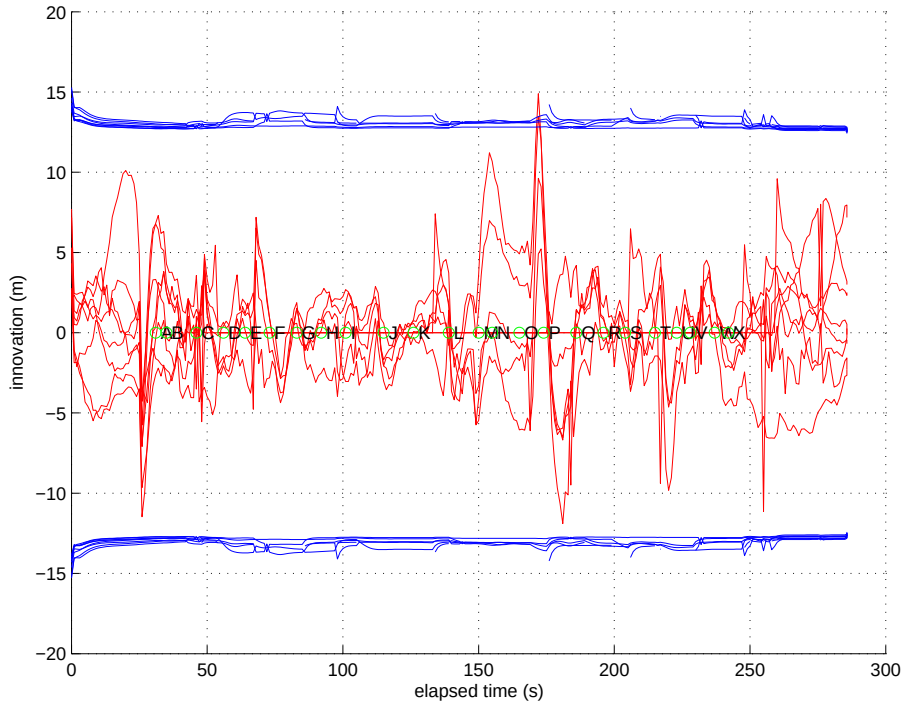


Figure 7.17: Innovation of the tightly-coupled filter for the entire run. In $e$-frame.

all these satellites (3-5 satellites, Sv nr.: 21, 18, 16, 15, 3) lies in north-west to south-east bound direction, indicating that the position estimate has a larger position error lateral to the direction of motion, which shows in Figure 7.16.

During the time-interval labels $T - W$ it can be seen in Figure 7.16 that the tightly-coupled filter estimated trajectory is very close to the reference GPS trajectory.The INS and GPS still conflict each other, but the estimated trajectory still manage the geometrical changes in the satellites. It should be noted that for this particular run no reference GPS measurements are available.

#### 7.2.2.2 Attitude Errors

Figure 7.20 shows the orientation of the vehicle during the entire run, plotted with the associated $3\sigma$ intervals. Just like in the loosely-coupled filter the attitude standard deviation for the pitch and roll estimates converge faster than the yaw estimate.all three error states, Figure 7.21.

The attitude estimation error of the filter, Figure 7.22, has been calculated as the difference between the navigation filter attitude angle estimates and the reference GPS attitude estimates. The only time where the reference measurements is valid is when the vehicle is stationary at the end of the experimental run. The pitch- and yaw-errors are in the order of 0.3° and 7° respectively at that time. Just like in the loosely-coupled filter there is a slow error growth in yaw error from 250 seconds when the car is standing still. The reason is that the Superstar II GPS do not contribute with heading information when it is stationary resulting in that the navigation filter has to rely on the inertial sensors with its increasing error.

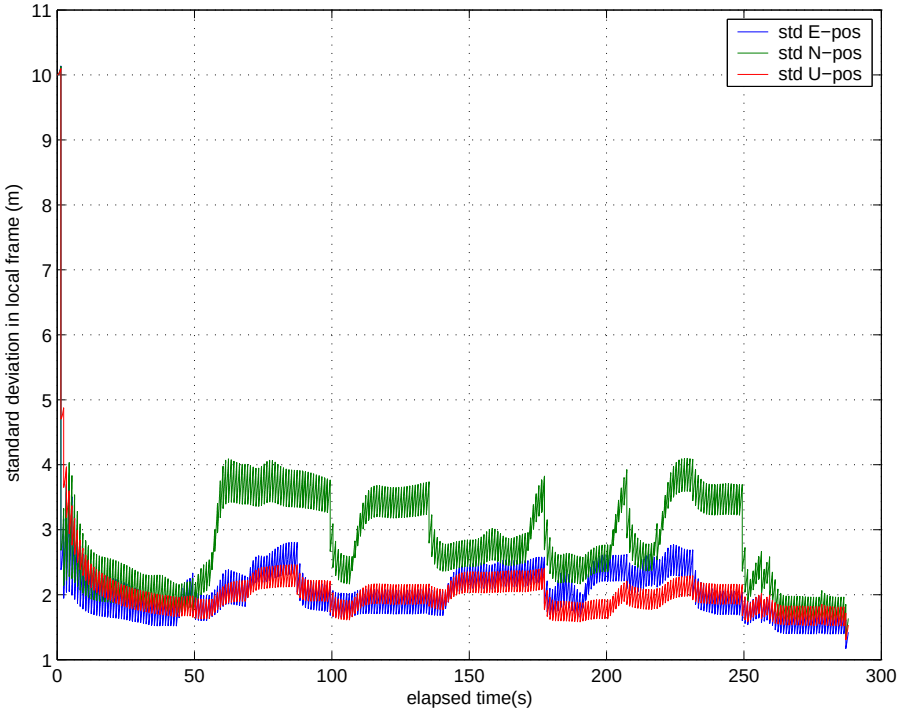


Figure 7.18: Standard deviation of the tightly-coupled filter position in a local frame.

#### 7.2.2.3 Gyro Bias

The initial value of the gyro bias and its covariance has been chosen according to Table 5.5 and 7.5, and is based on the calibration result presented in chapter 5. In Figure 7.23 and 7.24 it can clearly be seen that the roll- and pitch-gyro bias estimates converge faster than the yaw-gyro bias estimate, as in the loosely-coupled filter.

There are no changes in sign of the estimates and the estimates does not change radically from the initial guess originating from the calibration which indicates that the estimator is working properly.

By comparing the estimated gyro bias for the loosely-coupled, Figure 7.10, with the estimated gyro bias for the tightly-coupled filter, Figure 7.23, it can be seen that the estimates converge to the same values. This indicates that the gyro biases seems to be estimated correctly in the filters.

#### 7.2.2.4 Accelerometer Bias

The initial value of the accelerometer bias and its corresponding covariance has been chosen according to Table 5.1 and 7.5, and is based on the calibration result presented in chapter 5. In Figure 7.25 and 7.26 it clearly can be seen that the $x$- and $y$-accelerometer bias estimates converge slower than the $z$-accelerometer bias, as in the loosely-coupled filter.

Comparing the accelerometer bias estimates for the loosely-coupled filter, Figure 7.12, with the tightly-coupled estimated accelerometer bias, Figure 7.25, it can be seen that the estimates converge to the same vale indicting that the estimation of the filters is correct.

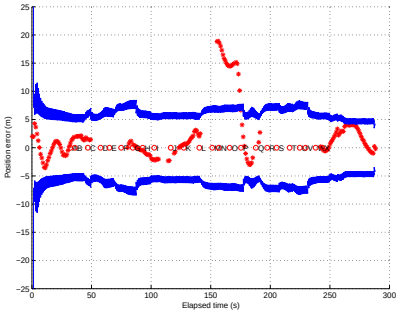


(a) Position estimation error in east (E) axis

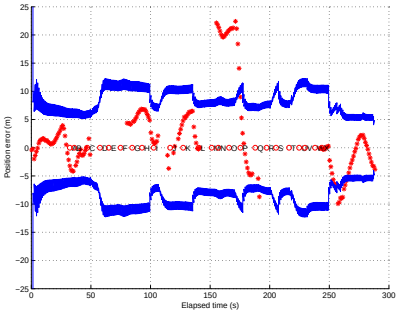


(b) Position estimation error in north (N) axis

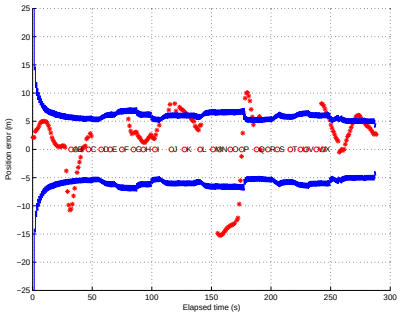


(c) Position estimation error in up (U) axis

Figure 7.19: Estimation error in position in a ENU local frame. The estimation errors in position are marked with red stars. Note that the estimation error is calculated as the difference between filter position and reference GPS position: lack of GPS reference data is the reason for the gaps in estimation error where it can not be evaluated.

#### 7.2.2.5 User Clock Error

Since the Superstar II GPS user clock is steered, meaning that the user clock is internally compensated for user clock errors, the user clock error should be fairly small and constant. This is also the case as seen in Figure 7.27. If the user clock was not steered the user clock bias would have a jagged shape like Figure 5.2 on page 151 in [9].

#### 7.2.2.6 Tightly Coupled Filter Using $10Hz$ Observations

Since the Superstar II receiver can produce pseudorange measurements at $10Hz$. Here follows a comparison between the $1Hz$ and the $10Hz$ solution. Figure 7.28 shows the accumulated error vector in position for both solutions. Since the reference attitude are not valid when the vehicle is moving, the accumulated error for the attitude can not be shown. Figure 7.29 shows the attitude errors instead.

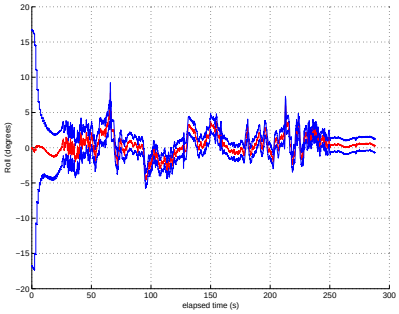


(a) Estimated roll angle.

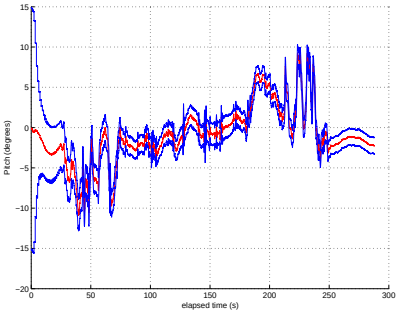


(b) Estimated pitch angle.

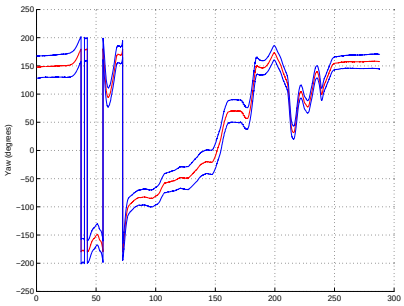


(c) Estimated yaw angle.

Figure 7.20: The estimated attitude angles expressed in the local frame with corresponding $3\sigma$ intervals.

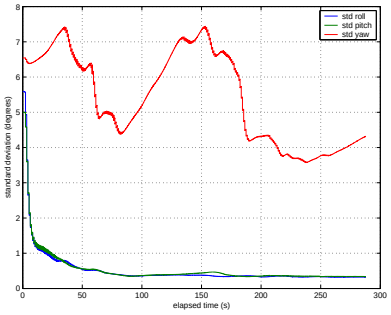


Figure 7.21: The standard deviation of the estimated attitude angles.

#### 7.2.2.7 Summary of Results for The Tightly Coupled Filter

The position error lies within the $3\sigma$ intervals for the major part of the test course. The filter has no problems when satellites loose tracking or are reacquired. The attitude estimates are good, but just like the position the yaw seems to drift when the vehicle is stationary. The gyro and accelerometer biases converge, and they converge to the same values as the loosely coupled biases. Just like expected the user clock bias was stable. Many things can be done to improve the result, like adding a velocity observation and expand the error modelling of the accelerometers and gyros.

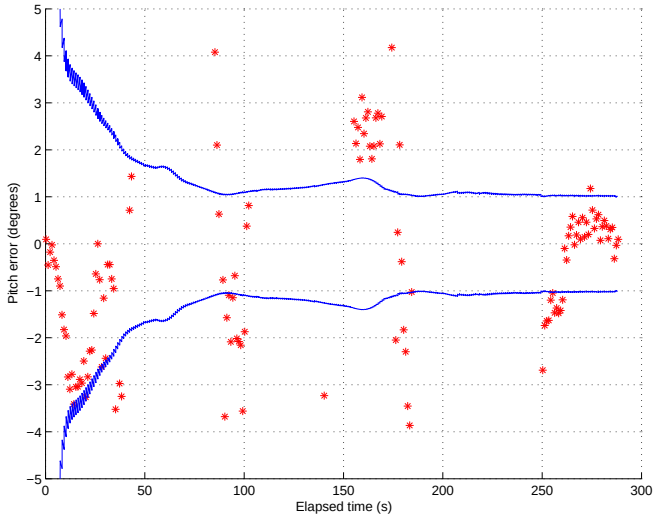


(a) Pitch error.

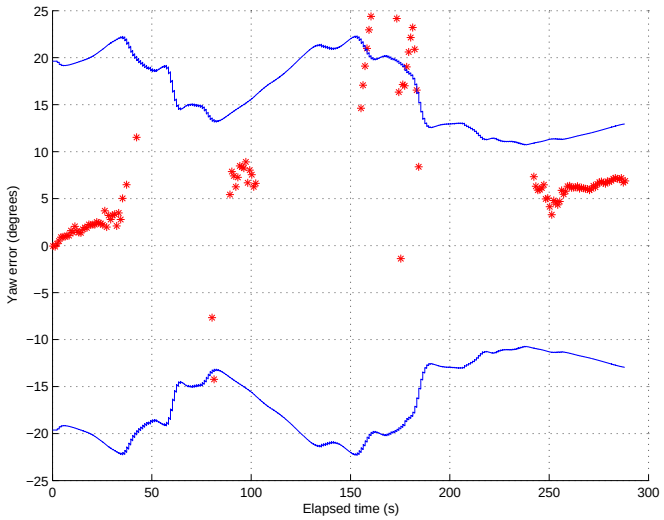


(b) Yaw error.

Figure 7.22: Estimation error in pitch and yaw with corresponding $3\sigma$ intervals.

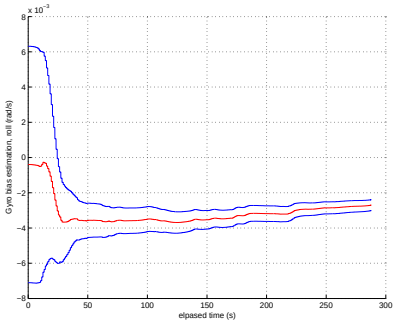


(a) Gyro bias for roll-gyro ($x$).

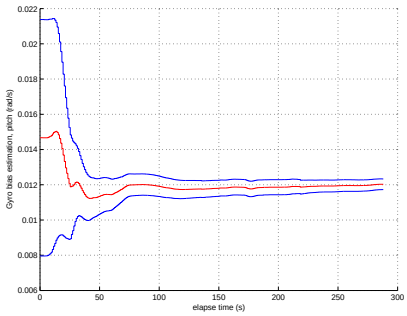


(b) Gyro bias for pitch-gyro ($y$).

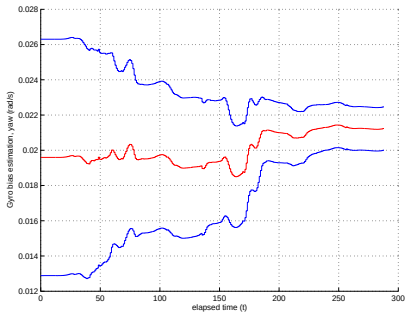


(c) Gyro bias for yaw-gyro ($z$).

Figure 7.23: Estimated gyro bias with corresponding $3\sigma$ intervals (rad/s).

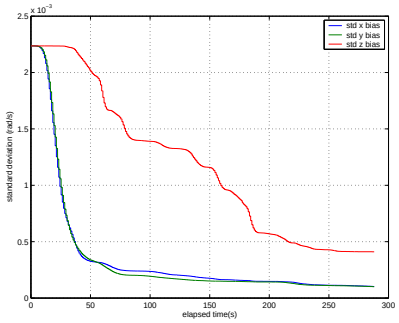


Figure 7.24: Standard deviation of the estimated gyro bias (rad/s).

## 7.3 Comparison Between Loosely and Tightly Coupled Filter Performance

Since the reference attitude can not be depended on, it is hard to make any conclusions on the performance of the attitude of the loosely and the tightly coupled filter. However the reference position can be trusted, and can therefore be used to compare the filter performance of the two integration techniques. Figure 7.30 and Figure 7.31 shows the filter positions plotted with the reference position for the loosely and the tightly coupled filter respectively. One can see that the loosely coupled filter does not have the same ability to coup with the

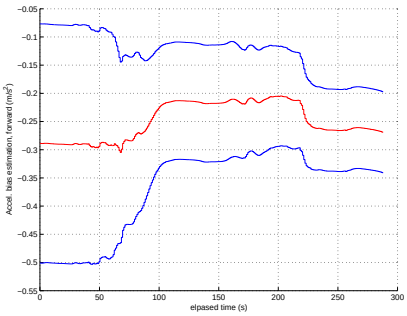


(a) Accelerometer bias estimate ward($x$).

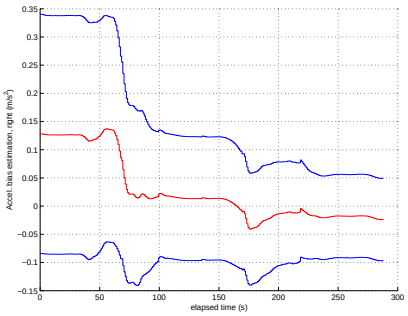


(b) Accelerometer bias estimate side($y$).

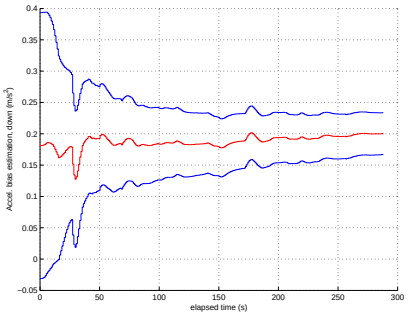


(c) Accelerometer bias estimate up($z$).

Figure 7.25: Estimated accelerometer bias in m/s$^2$.

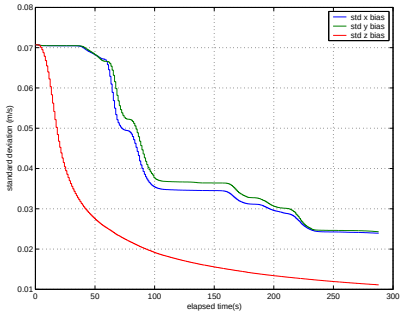


Figure 7.26: Standard deviation of the accelerometer bias in m/s$^2$.

sharp turn at the same time a new satellite appears, on the other hand the tightly coupled filter manage to follow the reference position fairly well. The conclusions that can be made is that the tightly coupled filter perform better under conditions where satellites loose tracking or are reacquired.

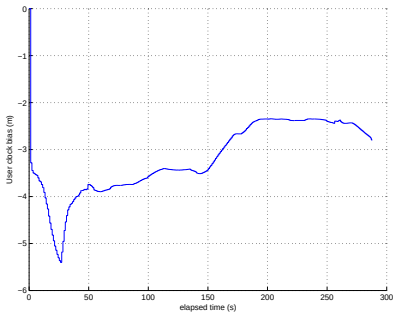


Figure 7.27: Estimated user clock bias in $m$.

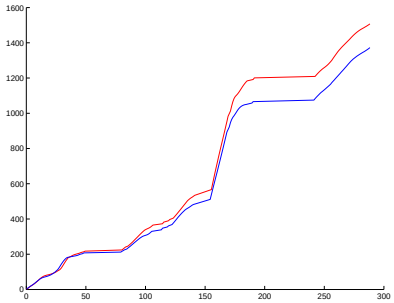

Figure 7.28: The accumulated error vector in position for the $1Hz$ and $10Hz$ solution. where the red line is the $1Hz$ solution and the blue line is the $10Hz$ solution.

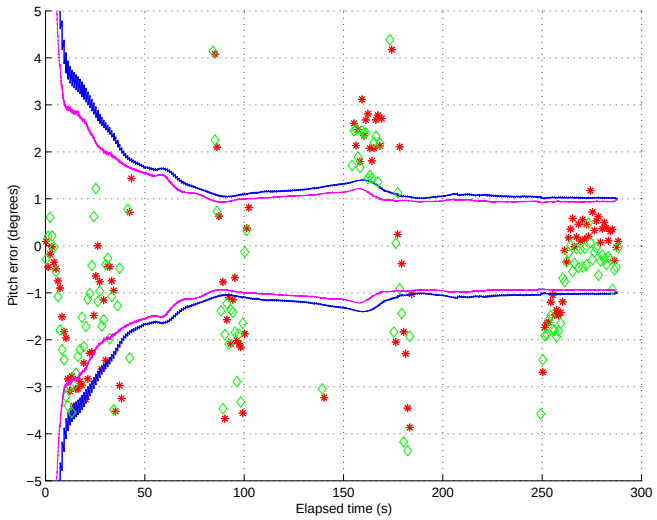


(a) Pitch error in degrees for entire run with 3 sigma limit

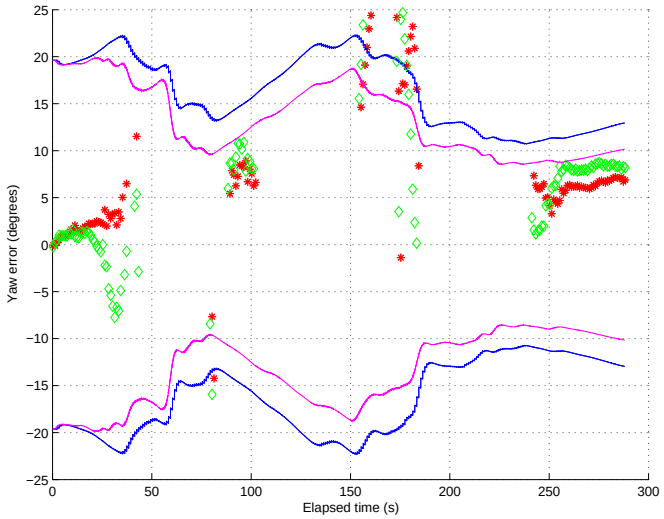


(b) Yaw error in degrees for entire run with 3 sigma limit

Figure 7.29: Attitude errors for the $1Hz$ (red stars and blue line) and $10Hz$ ( green stars and purple line) solution.

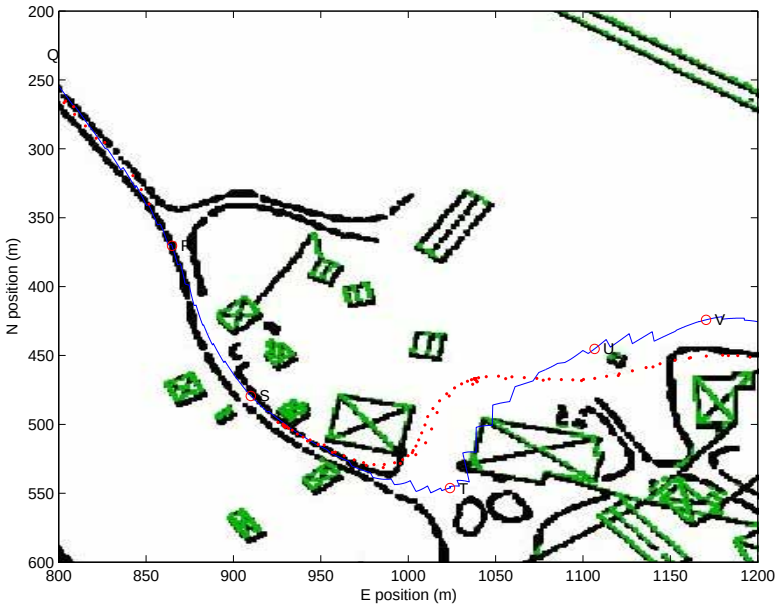


Figure 7.30: Estimated trajectory of the loosely-coupled filter in a local frame projected on a Ursvik map, plotted between labels $R - V$.

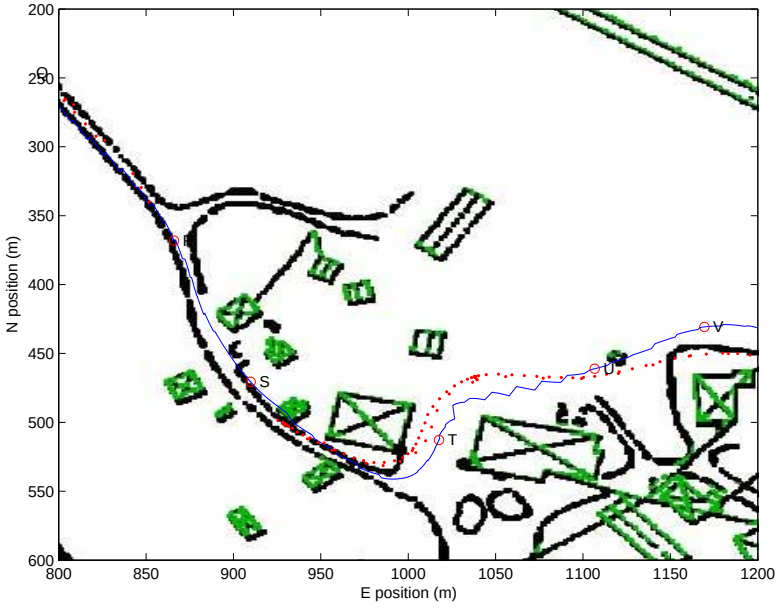


Figure 7.31: Estimated filter trajectory of the tightly-coupled filter in a local frame projected on a Ursvik map, plotted between labels $R - V$

# 8 Conclusions

The work consisted of designing and implementation of an integrated navigation platform based on a MEMS IMU and a GPS receiver. Also the data logging software for the PC 104 computer was implemented.

A comparison between a tight and a loose integration of a cheap MEMS IMU and a GPS, has been conducted on experimental data from a car driving in an environment with blocking buildings and dense foliage. Both navigation filters has been tuned and works well, except for cases when few satellites are available. Under these conditions the tightly integrated solution works the best.

Laboratory tests determining deterministic errors and stochastic IMU errors has been used to validate navigation filter performance by comparing the filter estimates with the corresponding calibrated errors. Initial high-dynamic tests in roller coaster showed a need for a better and more robust reference system to be able to validate the estimated position, velocity and in particular attitude.

It is also important, when having few available satellites, to have enough long data sets for the navigation filter to converge.

## 8.1 Future Work

Following below, is a list meassures which will improve the navigation algorithms and the validation process of the same.

### Experiments:

#### Reference System:

It is cruisal to use a more robust reference system that measures accurate position, velocity and attitude angles. It must also withstand high $g$'s, vibrations, impact and most important: longer periods of satellite outages.

By using doppler radar, wheel encoders and compass as reference measurements.

#### Satellite Availability:

The number of available satellites can be improved by a higher antenna placement to avoid damping or blocking from nearby objects. It is also important to plan experiments to be conducted during time intervals with as many satellites as possible.

#### Temperature:

When testing cheap MEMS-sensors it is important to either monitor the ambient temperature or to stabilize the same by temperature control or good insulation.

#### Trajectory:

It is advantegous to conduct multiple laps, Zero-velocity-updates (stopping for a certain time) and returning to a known point (start point) to be able to improve navigation performance by smart post-processing.

### Data logger:

The data logger can be improved by adding a checksum check. Improve the termination of the program. Look over the time stamping procedure and minimize the time stamping error. Create a better user interface.

### Navigation Filter:

#### Observation Model:

The observation model should be improved for both filters so that the observation also consist of velocity measurement.

#### System Model:

Improving the system model by incorporating all errors deducted through Allan variance analysis. Information about how to use Allan variance parameters in a Kalman filter can be found in [7] and [6].

#### Gravity Model:

The gravity model should be changed to a elliptic instead of a spherical.

#### Tropospheric Model:

The tropospheric model is now based on standard atmospheric parameters. The tropospheric model should be based on atmospheric parameters like air pressure, altitude, temperature, humidity corresponding to the actual situation.

#### Timing Aspects:

Now the filter syncronize the observation and prediction by taking the observation that is less then one IMU sampling period away. This may be improved by interpolating the prediction to the observation time.

# Bibliography

[1] *ICD200C, Navstar GPS Space Segment/Navigtion User Interfces.*

[2] *L1 GPS Firmware, Reference manual for NovAtel SUPERSTAR II-Based Products.*

[3] IEEE Std 1293-1998. Ieee standard specification format guide and test procedure for linear, single-axis, nongyroscopic accelerometersieee.

[4] IEEE Std 952-1997. Ieee standard specifiction format guide and test procedure for single -axis interferometric fiber optic gyros.

[5] Papoulis A. *Probability, Random Variables and Stochastic Processes.* McGraw-Hill Inc., 1991.

[6] A. J. Van Dierendonck J. B McGrw R. Grover Brown. Realtionship between allan variance and kalman filter parameters. In *16th Annul PTTI Applications and Planning Meeting*, 1984.

[7] Robert Grover Brown. *Introduction to Random Signals and Applied Kalman Filtering.* John Wiley and sons, 1997.

[8] Geoffrey J Bulmer. In *MICRO-ISU BP3010 An OEM Miniature Hybrid 6 Degrees-Of-Freedom Inertial Sensor Unit. Gyro Symposium, Stuttgart 16th-17th September*, 2003.

[9] Jay A. Farrell. *The Global Positioning System and inertial Navigation.* McGraw- Hill, 1998.

[10] Goldenberg. Gyro technology: Whats is on the horizon. In *ION NTM jan 2005.*

[11] Gyro, Accelerometer Panel of the IEEE Aerospace, and Electonic Systems Society. Draft recommended practice for inertial sensor test equipment, instrumentation, data acquisition, and anlysis. In *IEEE Std Working Draft P1554/D14.*

[12] Haiying Hou. Modeling inertial sensors errors using allan variance, ucege reports number 20201. Master's thesis, University of Calgary, September 2004.

[13] Christopher Jekeli. *Inertial Navigtion Systems With Geodetic Applications.* Walter de Gruyter, 2001.

[14] Johan Malmström. Robust navigation with gps/ins and adaptive beamforming, foi-r-0848-se. Master's thesis, FOI Swedish Defence Research Agency, 2003.

[15] Ingelstam; Rönngren and Sjöberg. *TEFYMA, Handbok för grundläggande teknisk fysik, fysik och matematik.* Sjöbergs förlag Stockholm/Bromma, 1984.

[16] Oleg S. Salychev. *Applied Inertial Navigation: Problems and Solutions*. BMSTU Press, Moscow Russia, 2004.

[17] Peter Strömbäck. Centralized gps/ins integration for urban navigation, foi-r-0847-se. Master's thesis, FOI, Swedish Defence Research Agency, 2003.

[18] David Titterton and John Weston. *Strapdown Inertial Navigtion Technology, 2nd Edition*. The Insitute of Electricl engineers IEE Radar, Sonar and Navigation series 17, 2004.

FOI is an assignment-based authority under the Ministry of Defence. The core activities are research, method and technology development, as well as studies for the use of defence and security. The organization employs around 1350 people of whom around 950 are researchers. This makes FOI the largest research institute in Sweden. FOI provides its customers with leading expertise in a large number of fields such as security-policy studies and analyses in defence and security, assessment of different types of threats, systems for control and management of crises, protection against and management of hazardous substances, IT-security an the potential of new sensors.

FOI
Swedish Defence Research Agency
SE-164 90 STOCKHOLM

Tel: +46 8 5550 3000
Fax: +46 8 5550 3100

www.foi.se